Published in final edited form as:
*Int j numer method biomed eng*. 2013 August ; 29(8): 822–849. doi:10.1002/cnm.2555.

# A Finite Element Based Constrained Mixture Implementation for Arterial Growth, Remodeling, and Adaptation: Theory and Numerical Verification

**A. Valentín**[1], **J. D. Humphrey**[2], and **G. A. Holzapfel**[1,3,*]

[1]Institute of Biomechanics, Center of Biomedical Engineering, Graz University of Technology, Kronesgasse 5-I, 8010 Graz, Austria

[2]Department of Biomedical Engineering, Yale University, New Haven CT 06520, USA

[3]Royal Institute of Technology (KTH), Department of Solid Mechanics, School of Engineering Sciences, Osquars Backe 1, 100 44 Stockholm, Sweden

## Abstract

We implemented a constrained mixture model of arterial growth and remodeling (G&R) in a nonlinear finite element framework to facilitate numerical analyses of diverse cases of arterial adaptation and maladaptation, including disease progression, resulting in complex evolving geometries and compositions. This model enables hypothesis testing by predicting consequences of postulated characteristics of cell and matrix turnover, including evolving quantities and orientations of fibrillar constituents and non-homogenous degradation of elastin or loss of smooth muscle function. The non-linear finite element formulation is general within the context of arterial mechanics, but we restricted our present numerical verification to cylindrical geometries to allow comparisons to prior results for two special cases: uniform transmural changes in mass and differential G&R within a two-layered cylindrical model of the human aorta. The present finite element model recovers the results of these simplified semi-inverse analyses with good agreement.

### Keywords

artery; stress; adaptation; mechanics

## 1 Introduction

Constrained mixture models of growth and remodeling (G&R) have seen increasing use in simulating chemomechanically driven cellular behaviors and their consequences in a variety of arterial analyses (Valentín and Holzapfel, 2012). However, most prior uses of this framework have been limited to simplified cases of axisymmetric motions or membrane approximations. Although such models have provided considerable insight, analysis of more realistic and diverse cases of arterial growth and remodeling requires that the framework be extended. Some more challenging problems include thick-walled, multi-layered arteries undergoing complex motions and subject to irregular boundary conditions, as in abdominal aortic aneurysms (AAAs). Naturally, increased attention has appropriately been directed towards developing traditional finite element models to compute both wall stress and the hemodynamics (Salsac *et al.*, 2004; Vorp, 2007). Nevertheless, AAAs are mechanically complex, biologically active lesions characterized by their evolving geometry, material

*Corresponding author (holzapfel@tugraz.at).

properties, and hemodynamic loads (Humphrey and Holzapfel, 2012). As with many areas of arterial mechanics, therefore, there is a pressing need for a 3-D finite element model capable of modeling the evolution of a multi-layered structure.

Generalizing the constrained mixture G&R framework entails several challenges. For example, the extent and mode of extracellular protein turnover and orientation require special attention. Care must be taken to ensure that convenient metrics driving G&R recover expected behaviors and special cases including, perhaps most crucially, tissue maintenance. In a three-dimensional model, the chemomechanical quantities driving G&R should consider 3-D field quantities, as opposed to just wall tension, as with membrane models, or mean intramural stress, as with some thick-walled models (Karšaj *et al.*, 2010; Valentín *et al.*, 2009). For complex motions, the alignment of newly-deposited fibers cannot be assumed to be constant and must also be described by an appropriate constitutive relation.

In this paper, we extend our prior advances in arterial G&R mechanics (cf., Baek *et al.*, 2006; Valentín *et al.*, 2009) via the development of a 3-D nonlinear finite element implementation within *FEAP* (Taylor, 2008). This framework includes all of the fundamental mechanisms of constrained mixture models and employs illustrative constitutive functions governing mass kinetics and fiber alignment (Baek *et al.*, 2006; Valentín and Humphrey, 2009a). Given the complexity of such a computational framework, however, the issue of verification is a natural concern (Anderson *et al.*, 2007). Thus, we verify the model for the special cases of homogenous changes of mass and differential G&R for a cylindrical geometry via comparison with results from a simpler semi-analytic model of G&R (Valentín *et al.*, 2011).

## 2 Methods

### 2.1 The Constrained Mixture Approach

We treat an artery as a constrained mixture and focus on mechanical contributions by the three primary structural constituents: elastic fibers, smooth muscle, and multiple families of locally parallel (at the time of production) collagen fibers. That is, we assume that each constituent $\alpha$ must deform with the artery as a whole, but otherwise may possess individual stress-free configurations, mechanical properties, and rates of turnover (Humphrey and Rajagopal, 2002). Employing a mass-averaged rule of mixtures approach to quantify the overall stored energy function $W=\sum_{\alpha} W^{\alpha}$ at each G&R time $s$, we let (Baek *et al.*, 2006; Valentín *et al.*, 2009)

$$W^{\alpha}(s)=\frac{\rho^{\alpha}(0)}{\rho(s)}\,Q^{\alpha}(s)\,\widehat{W}^{\alpha}\left(\mathbf{C}^{\alpha}_{\mathrm{n}(0)}(s)\right)+\int_{0}^{s}\frac{m^{\alpha}(\tau)}{\rho(s)}\,q^{\alpha}(s,\tau)\,\widehat{W}^{\alpha}\left(\mathbf{C}^{\alpha}_{\mathrm{n}(\tau)}(s)\right)\mathrm{d}\tau, \quad (1)$$

where $\rho^{\alpha}(0)$ is the constituent mass density (per constant unit reference volume) at $s = 0$, just prior to the commencement of G&R, $Q^{\alpha}(s) \in [0, 1]$ is the fraction of constituent $\alpha$ that was present at $s = 0$ that survives to time $s$, $m^{\alpha}(\tau)$ is the rate of production of constituent $\alpha$ at time $\tau \in [0, s]$, $q^{\alpha}(s, \tau) \in [0, 1]$ is the fraction of constituent $\alpha$ that was produced at time $\tau$ that survives to time $s$, and $\widehat{W}^{\alpha}$ is the stored energy for a cohort of constituent $\alpha$, which depends on the individual right Cauchy-Green tensor

$$\mathbf{C}^{\alpha}_{\mathrm{n}(\tau)}(s)=\left(\mathbf{F}^{\alpha}_{\mathrm{n}(\tau)}(s)\right)^{\mathrm{T}}\mathbf{F}^{\alpha}_{\mathrm{n}(\tau)}(s), \quad (2)$$

where (Baek *et al.*, 2005)

$$\mathbf{F}^{\alpha}_{\mathrm{n}(\tau)}(s)=\mathbf{F}(s)\,\mathbf{F}^{-1}(\tau)\,\mathbf{G}^{\alpha}(\tau). \quad (3)$$

The subscript n($\tau$) (or, n($\tau = 0$)) denotes the individual stress-free (natural) configuration for a cohort of constituent $\alpha$ at the time $\tau$ it was produced. Note, too, that $\mathbf{G}^{\alpha}(\tau)$ denotes the 'deposition stretch tensor' that captures the prestretch at which the constituent was incorporated within the extant extracellular matrix whereas $\mathbf{F}(s)$ and $\mathbf{F}(\tau)$ denote overall deformation gradient tensors that account for motions by the artery from a convenient (measurable) reference configuration at time $s = 0$ to subsequent configurations at times $s$ and $\tau$, respectively. Thus, $\mathbf{F}(s)\,\mathbf{F}^{-1}(\tau)$ represents the overall *in vivo* deformation of the artery from the time $\tau$ of constituent production to the current time $s$. Finally, $\rho(s)$ is the overall mass density of the artery at time $s$, where $\rho(s)=\sum_{\alpha}\rho^{\alpha}(s)$, and

$$\rho^{\alpha}(s)=\rho^{\alpha}(0)\,Q^{\alpha}(s)+\int_{0}^{s} m^{\alpha}(\tau)\,q^{\alpha}(s,\tau)\,\mathrm{d}\tau. \quad (4)$$

Clearly, $\sum_{\alpha}\rho^{\alpha}(s)/\rho(s) \equiv \sum_{\alpha}\phi^{\alpha}(s) \equiv 1$ where $\phi^{\alpha}(s)$ are potentially evolving mass fractions; also $Q^{\alpha}(0) = 1$, by definition. Finally, an important feature of this G&R framework is that the production ($m^{\alpha}(\tau)$) and survival ($q^{\alpha}(s, \tau)$) functions that govern constituent turnover may depend on diverse chemical (e.g., growth factors or proteases) and mechanical (chiefly stress or tension) stimuli sensed by the appropriate cell type.

## 2.2 General Constitutive Framework

Prior constrained mixture G&R analyses have focused on idealized geometries and/or exploited membrane assumptions (see Valentín and Holzapfel, 2012, for a review), hence there is a pressing need for a generalized framework that can be used to analyze more diverse initial-boundary value problems. Given complexity in geometry, mechanical behavior, and loading inherent in many problems in vascular mechanics, and consistent with traditional biomechanical analyses, we employ the finite element method. Also, consistent with many implementations of the finite element method in finite elasticity, we employ a volumetric/distortional split of the stored energy function, which required a reformulation of the constrained mixture formulation. This change led, in turn, to the introduction of a different metric to drive G&R, which we feel is important in three dimensional problems.

**2.2.1 Stress—**Despite different rates of turnover by individual constituents and hence changes in constituent mass densities or mass fractions, it appears that the overall spatial mass density $\rho$ remains nearly constant (~ 1050 kg · m$^{-3}$) in most cases of arterial adaptations. Consequently, overall mass and volume mostly change together. Nevertheless, it also appears that at a given G&R time $s$, arterial behavior in response to transient loading (e.g., *in vivo* during the cardiac cycle or *in vitro* during typical biaxial mechanical testing) is nearly isochoric. Hence, a general finite element formulation must allow large changes in mass or volume while enforcing the incompressibility constraint common in arterial mechanics (Humphrey, 2002). These two motivations prompted us to adapt classical approaches from hyperelasticity to develop and implement a constrained mixture model of G&R within a finite element framework. The total evolving elastic stored energy, defined per unit volume in the referential, healthy state, is thus written in the decoupled form (Holzapfel and Weizsäcker, 1998)

$$W(\mathbf{C}(s))=W_{\mathrm{vol}}(J(s))+W_{\mathrm{dis}}(\overline{\mathbf{C}}(s)), \quad (5)$$

where $W_{\text{vol}}(J(s))$ is the elastic contribution due to departures from a specified volume (increases, in the case of growth, or decreases, in the case of atrophy), $J(s) = \det \mathbf{F}(s)$ is the ratio of current to original differential volumes, and $W_{\text{dis}}(\bar{\mathbf{C}}(s))$ is the elastic contribution due to isochoric distortions. $\bar{\mathbf{C}}(s) = J^{-2/3}(s)\,\mathbf{C}(s)$ is the so-called 'modified' right Cauchy-Green tensor, where $\bar{\mathbf{C}}(s) = \bar{\mathbf{F}}^{\mathrm{T}}(s)\,\bar{\mathbf{F}}(s)$. This approach stems from Flory's (1961) concept of a multiplicative decomposition of the deformation gradient tensor into dilatational and distortional components, namely $\mathbf{F}(\cdot) = (J^{1/3}(\cdot)\,\mathbf{I})\,\bar{\mathbf{F}}(\cdot)$ where $\bar{\mathbf{F}}(\cdot)$ is a modified deformation gradient tensor where $\det \bar{\mathbf{F}}(\cdot) \equiv 1$, and $\mathbf{I} = \delta_{ij}\,\mathbf{e}_i \otimes \mathbf{e}_j$ is the second-order identity tensor, the operator $\otimes$ denotes the tensor (dyadic) product, and $\delta_{ij}$ is the Kronecker delta.

The additive volumetric-distortional split in equation (5) permits us to write the second Piola-Kirchhoff stress tensor as the sum of spherical and distortional elastic contributions plus, as in the case of arteries, an active stress contribution

$$\mathbf{S}(s) = \mathbf{S}_{\text{sph}}(s) + \mathbf{S}_{\text{dis}}(s) + \mathbf{S}_{\text{act}}(s). \quad (6)$$

The spherical portion is

$$\mathbf{S}_{\text{sph}}(s) = J(s)\,p(s)\,\mathbf{C}^{-1}(s), \qquad p(s) = \frac{\mathrm{d}W_{\text{vol}}(J(s))}{\mathrm{d}J(s)}, \quad (7)$$

where $p(s)$ is a Lagrange multiplier; $\mathbf{S}_{\text{sph}}(s)$ is sometimes also called the volumetric component of the second Piola-Kirchhoff stress tensor. The contribution of the second Piola-Kirchhoff stress tensor resulting from the distortional elastic response is

$$\mathbf{S}_{\text{dis}}(s) = 2\frac{\partial W_{\text{dis}}(\bar{\mathbf{C}}(s))}{\partial \mathbf{C}(s)}. \quad (8)$$

**2.2.2 Stiffness—**The stiffness tensor (also known as the tangent modulus or elasticity tensor), required for iterative solution of nonlinear problems via the finite element method, may also be decomposed into spherical, distortional, and active contributions (cf. Holzapfel, 2000, Ch. 6.6)

$$\mathbb{C}(s) = \mathbb{C}_{\text{sph}}(s) + \mathbb{C}_{\text{dis}}(s) + \mathbb{C}_{\text{act}}(s). \quad (9)$$

where the contribution resulting from volumetric dilatations is

$$\mathbb{C}_{\text{sph}}(s) = J(s)\,\tilde{p}(s)\,\mathbf{C}^{-1}(s) \otimes \mathbf{C}^{-1}(s) + 2J(s)\,p(s)\,\frac{\partial \mathbf{C}^{-1}(s)}{\partial \mathbf{C}(s)}, \qquad \tilde{p}(s) = p(s) + J(s)\,\frac{\mathrm{d}p(s)}{\mathrm{d}J(s)}. \quad (10)$$

The contribution resulting from isochoric distortions is

$$\begin{aligned}\mathbb{C}_{\text{dis}}(s) \;=\; & \mathbf{P}(s) : \bar{\mathbb{C}}(s) : \mathbf{P}^{\mathrm{T}}(s) \\ & + \tfrac{2}{3}\,J^{-2/3}(s)\,\{\bar{\mathbf{S}}(s) : \mathbf{C}(s)\}\,\tilde{\mathbf{P}}(s) - \tfrac{2}{3}\,(\mathbf{C}^{-1}(s) \otimes \mathbf{S}_{\text{dis}}(s) + \mathbf{S}_{\text{dis}}(s) \otimes \mathbf{C}^{-1}(s)),\end{aligned} \quad (11)$$

where the ' : ' operator denotes a double contraction (inner product). The so-called 'fictitious' second Piola-Kirchhoff stress tensor and associated stiffness tensor are

$$\bar{\mathbf{S}}(s) = 2\,\frac{\partial W_{\text{dis}}(\bar{\mathbf{C}}(s))}{\partial \bar{\mathbf{C}}(s)}, \qquad \bar{\mathbb{C}}(s) = 4\,J^{-4/3}(s)\,\frac{\partial^2 W_{\text{dis}}(\bar{\mathbf{C}}(s))}{\partial \bar{\mathbf{C}}(s)\,\partial \bar{\mathbf{C}}(s)}. \quad (12)$$

respectively. The projection tensor and its transpose are simply

$$\mathrm{P}(s)=\mathbf{I}-\tfrac{1}{3}\mathbf{C}^{-1}(s)\otimes\mathbf{C}(s),\qquad \mathrm{P}^{\mathrm{T}}(s)=\mathbf{I}-\tfrac{1}{3}\mathbf{C}(s)\otimes\mathbf{C}^{-1}(s),\quad (13)$$

where $\mathbf{I}=\delta_{ik}\,\delta_{jl}\,\mathbf{e}_i\otimes\mathbf{e}_j\otimes\mathbf{e}_k\otimes\mathbf{e}_l$ is the fourth order identity tensor, and the modified projection tensor is

$$\tilde{\mathrm{P}}(s)=-\frac{\partial\mathbf{C}^{-1}(s)}{\partial\mathbf{C}(s)}-\frac{1}{3}\mathbf{C}^{-1}(s)\otimes\mathbf{C}^{-1}(s).\quad (14)$$

**2.2.3 Spatial descriptors—**Whereas the second Piola-Kirchhoff stress is useful constitutively, final results are best appreciated in terms of the Cauchy stress. Via a standard 'push-forward' operation, the Cauchy stress tensor is

$$\sigma(s)=J^{-1}(s)\,\mathbf{F}(s)\,\mathbf{S}(s)\,\mathbf{F}^{\mathrm{T}}(s).\quad (15)$$

It is useful to delineate deviatoric and constituent-specific distortional contributions to the Cauchy stress tensor, namely

$$\sigma_{\mathrm{dev}}(s)=J^{-1}(s)\,\mathbf{F}(s)\,(\mathbf{S}_{\mathrm{dis}}(s)+\mathbf{S}_{\mathrm{act}}(s))\,\mathbf{F}^{\mathrm{T}}(s)=\sigma(s)-\frac{1}{3}\,\mathrm{tr}\,\sigma(\mathrm{s})\,\mathbf{I},\quad (16)$$

and

$$\sigma^{\alpha}_{\mathrm{dis}}(s)=J^{-1}(s)\,\mathbf{F}(s)\,\mathbf{S}^{\alpha}_{\mathrm{dis}}(s)\,\mathbf{F}^{\mathrm{T}}(s),\quad (17)$$

where (cf., equation (8)) $\mathbf{S}^{\alpha}_{\mathrm{dis}}(s)=2\,\partial W^{\alpha}_{\mathrm{dis}}(\overline{\mathbf{C}}(s))/\partial\mathbf{C}(s)$. The associated spatial form of the stiffness tensor is obtained via a Piola transformation and can be represented in index notation following Einstein's summation convention

$$c_{ijkl}(s)=J^{-1}(s)\,F_{iA}(s)\,F_{jB}(s)\,F_{kC}(s)\,F_{lD}(s)\,C_{ABCD}(s),\quad (18)$$

where $C_{ABCD}(s)$ are the components of the stiffness tensor from equation (9).

## 2.3 Illustrative Constitutive Relations

To illustrate the utility of a finite element based G&R framework and to verify the numerical implementation, we must prescribe constitutive relations for elastic and active responses, rates of production, and removal kinetics (cf., equations (1), (4), and (6)). Although significantly more work must continue both to collect the requisite data and to improve the functional forms, considerable progress has been achieved in recent years, and current forms yield salient responses in many cases. We employ available relations to illustrate the utility of the present implementation. Because of the spherical-distortional split, some prior relations and/or their parameters appear here in their modified forms.

**2.3.1 Volumetric stored energy—**Contributions to the overall stored energy due to departures in volume from $J_{\mathrm{his}}(s)=\rho(s^{-})/\rho(0)$, which captures dilatational changes due to the histories of possible growth or atrophy and where $s^{-}$ represents the prior time step, is written as (Holzapfel, 2000)

$$W_{\mathrm{vol}}(J(s))=\frac{K(J(s))}{2}\{J(s)-J_{\mathrm{his}}(s)\}^{2},\quad (19)$$

where $K(J(s))$ is a growth dependent bulk modulus that serves as a penalty function. To aid convergence, we require that $\lim_{J\to 0} K(J)=\infty$ and thus postulate

$$K(J(s))=\begin{cases} K_0\, J^{-\beta}(s) & \forall J(s)\in(0,1), \\ K_0 & \forall J(s)\in[1,\infty), \end{cases} \quad (20)$$

where $K_0 = 100$ MPa, and $\beta \geq 1$ is a dimensionless parameter (figure 1). This penalty function enforces incompressibility numerically during transient motions while simultaneously satisfying boundary conditions.

**2.3.2 Elastin—**We employ a neo-Hookean stored energy function for elastin (Dorrington and McCrum, 1977; Holzapfel *et al.*, 2000)

$$\widehat{W}^{\mathrm{e}}(s)=\frac{c^{\mathrm{e}}(s)}{2}(\mathrm{tr}\,\mathbf{C}^{\mathrm{e}}(s)-3), \quad (21)$$

where $c^{\mathrm{e}}(s)$ is a potentially evolving shear modulus, $\mathbf{C}^{\mathrm{e}}(s)=(\mathbf{F}^{\mathrm{e}}(s))^{\mathrm{T}}\,\mathbf{F}^{\mathrm{e}}(s)$, $\mathbf{F}^{\mathrm{e}}(s)=\mathbf{F}(s)\,\tilde{\mathbf{G}}^{\mathrm{e}}$, and $\tilde{\mathbf{G}}^{\mathrm{e}}$ is a positive definite prestretch tensor that describes isochoric motions experienced by the elastin from its natural (unstressed) configuration to the reference configuration at time $s = 0$. Hence, $\tilde{\mathbf{G}}^{\mathrm{e}}$ accounts both for original deposition stretches and development related stretches incurred because of the long half-life of elastin. Because elastin is not continuously produced in maturity (at intermediate times $\tau$), there is no need to map motions back to a stress-free configuration $\mathrm{n}(\tau)$. For a cylindrical geometry, this prestretch tensor, in matrix notation, is

$$\left[\tilde{\mathbf{G}}^{\mathrm{e}}\right]_{(r,\theta,z)}=\mathrm{diag}\left[\left(\tilde{G}^{\mathrm{e}}_{\theta\theta}\,\tilde{G}^{\mathrm{e}}_{zz}\right)^{-1},\tilde{G}^{\mathrm{e}}_{\theta\theta},\tilde{G}^{\mathrm{e}}_{zz}\right]. \quad (22)$$

In general, $\tilde{\mathbf{G}}^{\mathrm{e}}$ may vary with radial position (Cardamone *et al.*, 2009). Using the above relations, we can write $\mathbf{C}^{\mathrm{e}}(s)=(\tilde{\mathbf{G}}^{\mathrm{e}})^{\mathrm{T}}\,\mathbf{C}(s)\,\tilde{\mathbf{G}}^{\mathrm{e}}$. Recalling that equation (8) calls for 'isochoric' functions for stored energy (elastic responses due to local isochoric distortions), we can rewrite equation (21) as a function of the modified first invariant $\overline{I}^{\mathrm{e}}_1$, namely

$$\widehat{W}^{\mathrm{e}}_{\mathrm{dis}}(s)=\frac{c^{\mathrm{e}}(s)}{2}\left(\overline{I}^{\mathrm{e}}_1(s)-3\right), \quad (23)$$

where $\overline{I}^{\mathrm{e}}_1(s)=\mathrm{tr}\,\overline{\mathbf{C}}^{\mathrm{e}}(s)$, and $\overline{\mathbf{C}}^{\mathrm{e}}(s)=J^{-2/3}(s)\,\mathbf{C}^{\mathrm{e}}(s)$. Thus, for prestretched elastin,

$$\frac{\partial\widehat{W}^{\mathrm{e}}_{\mathrm{dis}}\left(\overline{I}^{\mathrm{e}}_1(s)\right)}{\partial\mathbf{C}(s)}=\frac{\partial\widehat{W}^{\mathrm{e}}_{\mathrm{dis}}\left(\overline{I}^{\mathrm{e}}_1(s)\right)}{\partial\overline{I}^{\mathrm{e}}_1(s)}\frac{\partial\overline{I}^{\mathrm{e}}_1(s)}{\partial\mathbf{C}(s)}, \quad (24)$$

where (see Appendix 1)

$$\frac{\partial\widehat{W}^{\mathrm{e}}_{\mathrm{dis}}\left(\overline{I}^{\mathrm{e}}_1(s)\right)}{\partial\overline{I}^{\mathrm{e}}_1(s)}=\frac{c^{\mathrm{e}}(s)}{2}, \quad \frac{\partial\overline{I}^{\mathrm{e}}_1(s)}{\partial\mathbf{C}(s)}=J^{-2/3}(s)\left(\tilde{\mathbf{G}}^{\mathrm{e}}\left(\tilde{\mathbf{G}}^{\mathrm{e}}\right)^{\mathrm{T}}-\frac{1}{3}\mathrm{tr}\,\mathbf{C}^{\mathrm{e}}(s)\,\mathbf{C}^{-1}(s)\right). \quad (25)$$

Finally, we note that equation $(12)_1$ calls for the quantity

$$\frac{\partial \widehat{W}^{\mathrm{e}}_{\mathrm{dis}}\left(\overline{I}^{\mathrm{e}}_{1}(s)\right)}{\partial \overline{\mathbf{C}}(s)}=\frac{\partial \widehat{W}^{\mathrm{e}}_{\mathrm{dis}}\left(\overline{I}^{\mathrm{e}}_{1}(s)\right)}{\partial \overline{I}^{\mathrm{e}}_{1}(s)}\frac{\partial \overline{I}^{\mathrm{e}}_{1}(s)}{\partial \overline{\mathbf{C}}(s)}, \quad (26)$$

where, similar to equation (A.6)

$$\frac{\partial \overline{I}^{\mathrm{e}}_{1}(s)}{\partial \overline{\mathbf{C}}(s)}=\tilde{\mathbf{G}}^{\mathrm{e}}\left(\tilde{\mathbf{G}}^{\mathrm{e}}\right)^{\mathrm{T}}. \quad (27)$$

Note that for the case of a neo-Hookean material, $\bar{\mathbb{C}}(s) = \mathrm{O}$, which is the fourth order zero tensor.

**2.3.3 Collagen and passive muscle—**Next, consider the stored energy for a cohort of fibrillar constituents: passive smooth muscle, denoted by superscript 'm', and four families of collagen, denoted by superscript '*k*' (m, $k = 1, 2, 3, 4$), which, in contrast to elastin, are continuously synthesized and degraded in maturity. Following Holzapfel *et al.* (2000), we employ the form

$$\widehat{W}^{\alpha}(s)=\frac{c^{\alpha}_{2}(s)}{4\,c^{\alpha}_{3}}\left[\exp\left(c^{\alpha}_{3}\left\{\lambda^{\alpha}_{\mathrm{n}(\tau)}(s)^{2}-1\right\}^{2}\right)-1\right] \quad (28)$$

and recall the series of linear transformations that describe motions from the natural configuration for constituent $\alpha$ at the time of deposition $\tau$ to the current *in vivo* configuration at time $s$. In addition, recall equation (3), where $\mathbf{G}^{\alpha}(\tau)=G^{\alpha}_{\mathrm{h}}(\tau)\,\mathbf{m}^{\alpha}(\tau)\otimes\mathbf{m}^{\alpha}(\tau)$ is a structural tensor describing the state of prestretch for a fibrillar constituent oriented along unit vector $\mathbf{m}^{\alpha}(\tau)$, and $G^{\alpha}_{\mathrm{h}}(\tau)$ may be interpreted as the homeostatic stretch imposed on an individual fiber by synthesizing cells during secretion and subsequent incorporation within the extracellular matrix. $\mathbf{G}^{\alpha}(\tau)$ may also be conceptualized as a linear transformation (specifically, a projection) such that (cf. Baek *et al.*, 2006)

$$\mathbf{G}^{\alpha}(\tau)\,\mathbf{M}^{\alpha}_{\mathrm{n}(\tau)}=G^{\alpha}_{\mathrm{h}}(\tau)\,\mathbf{m}^{\alpha}(\tau), \quad (29)$$

where the fiber is coaxial with unit vector $\mathbf{M}^{\alpha}_{\mathrm{n}(\tau)}$ in its natural configuration, which exists conceptually, but cannot be realized experimentally. Because $\mathbf{M}^{\alpha}_{\mathrm{n}(\tau)}$ is of unit length, then $\mathbf{M}^{\alpha}_{\mathrm{n}(\tau)}\equiv\mathbf{m}^{\alpha}(\tau)$. This formulation thereby facilitates naturally the inclusion of experimental observations, that is, measurements from *in vivo* or *ex vivo* experiments regarding microstructural information and inferences regarding prestretches. The total stretch experienced by a fiber from its natural configuration at time $\tau$ to the current configuration at time $s$ is

$$\lambda^{\alpha}_{\mathrm{n}(\tau)}(s)=\left\{\eta^{\alpha}(\tau)\cdot\mathbf{C}(s)\,\eta^{\alpha}(\tau)\right\}^{1/2}, \quad (30)$$

or, more concisely as the fourth invariant $I^{\alpha}_{4_{\mathrm{n}(\tau)}}(s)=\eta^{\alpha}(\tau)\cdot\mathbf{C}(s)\,\eta^{\alpha}(\tau)$, where $\eta^{\alpha}(\tau)=\mathbf{F}^{-1}(\tau)\,\mathbf{G}^{\alpha}(\tau)\,\mathbf{M}^{\alpha}_{\mathrm{n}(\tau)}\equiv\mathbf{M}^{\alpha}_{\mathrm{n}(\tau)}\left(\mathbf{F}^{-1}(\tau)\,\mathbf{G}^{\alpha}(\tau)\right)^{\mathrm{T}}$, since a vector and its transpose are equal when written in direct notation.

Recalling the definition of the modified deformation gradient tensor, we have the analog $\overline{\eta^{\alpha}}(\tau)=J^{-1/3}(\tau)\,\eta^{\alpha}(\tau)$ and can write the modified fourth invariant

$$\overline{I^{\alpha}_{4_{n(\tau)}}}(s)=\overline{\eta^{\alpha}}(\tau)\cdot\overline{\mathbf{C}}(s)\,\overline{\eta^{\alpha}}(\tau)=J^{-2/3}(s)\,\overline{\eta^{\alpha}}(\tau)\cdot\mathbf{C}(s)\,\overline{\eta^{\alpha}}(\tau). \quad (31)$$

The stored energy resulting from isochoric distortions is then

$$\widehat{W}^{\alpha}_{\text{dis}}(s)=\frac{c^{\alpha}_{2}(s)}{4\,c^{\alpha}_{3}}\left[\exp\left(c^{\alpha}_{3}\left\{\overline{I^{\alpha}_{4_{n(\tau)}}}(s)-1\right\}^{2}\right)-1\right]. \quad (32)$$

We can use the chain rule to write

$$\frac{\partial\widehat{W}^{\alpha}_{\text{dis}}\left(\overline{I^{\alpha}_{4_{n(\tau)}}}(s)\right)}{\partial\mathbf{C}(s)}=\frac{\partial\widehat{W}^{\alpha}_{\text{dis}}\left(\overline{I^{\alpha}_{4_{n(\tau)}}}(s)\right)}{\partial\overline{I^{\alpha}_{4_{n(\tau)}}}(s)}\frac{\partial\overline{I^{\alpha}_{4_{n(\tau)}}}(s)}{\partial\mathbf{C}(s)}, \quad (33)$$

where (see Appendix 2)

$$\frac{\partial\widehat{W}^{\alpha}_{\text{dis}}\left(\overline{I^{\alpha}_{4_{n(\tau)}}}(s)\right)}{\partial\overline{I^{\alpha}_{4_{n(\tau)}}}(s)}=\frac{c^{\alpha}_{2}(s)}{2}\left\{\overline{I^{\alpha}_{4_{n(\tau)}}}(s)-1\right\}\exp\left(c^{\alpha}_{3}\left\{\overline{I^{\alpha}_{4_{n(\tau)}}}(s)-1\right\}^{2}\right), \quad (34)$$

$$\frac{\partial\overline{I^{\alpha}_{4_{n(\tau)}}}(s)}{\partial\mathbf{C}(s)}=J^{-2/3}(s)\,\overline{\eta^{\alpha}}(\tau)\otimes\overline{\eta^{\alpha}}(\tau)-\frac{1}{3}\overline{I^{\alpha}_{4_{n(\tau)}}}(s)\,\mathbf{C}^{-1}(s). \quad (35)$$

The contribution to equation $(12)_1$ by fibrillar cohorts can be written

$$\frac{\partial\widehat{W}^{\alpha}_{\text{dis}}\left(\overline{I^{\alpha}_{4_{n(\tau)}}}(s)\right)}{\partial\overline{\mathbf{C}}(s)}=\frac{\partial\widehat{W}^{\alpha}_{\text{dis}}\left(\overline{I^{\alpha}_{4_{n(\tau)}}}(s)\right)}{\partial\overline{I^{\alpha}_{4_{n(\tau)}}}(s)}\frac{\partial\overline{I^{\alpha}_{4_{n(\tau)}}}(s)}{\partial\overline{\mathbf{C}}(s)}, \quad (36)$$

where, similar to equation (A.7),

$$\frac{\partial\overline{I^{\alpha}_{4_{n(\tau)}}}(s)}{\partial\overline{\mathbf{C}}(s)}=\overline{\eta^{\alpha}}(\tau)\otimes\overline{\eta^{\alpha}}(\tau). \quad (37)$$

Finally, the contribution to equation $(12)_2$ by fibrillar cohorts can be written

$$\frac{\partial^{2}\widehat{W}^{\alpha}_{\text{dis}}\left(\overline{I^{\alpha}_{4_{n(\tau)}}}(s)\right)}{\partial\overline{\mathbf{C}}(s)\,\partial\overline{\mathbf{C}}(s)}=\Omega^{\alpha}(s,\tau)\,\overline{\eta^{\alpha}}(\tau)\otimes\overline{\eta^{\alpha}}(\tau)\otimes\overline{\eta^{\alpha}}(\tau)\otimes\overline{\eta^{\alpha}}(\tau), \quad (38)$$

with

$$\Omega^{\alpha}(s,\tau)=\frac{c^{\alpha}_{2}(s)}{2}\left(2\,c^{\alpha}_{3}\left\{\overline{I^{\alpha}_{4_{n(\tau)}}}(s)-1\right\}^{2}+1\right)\exp\left(c^{\alpha}_{3}\left\{\overline{I^{\alpha}_{4_{n(\tau)}}}(s)-1\right\}^{2}\right). \quad (39)$$

**2.3.4 Active generation of stress—**In contrast to $\mathbf{S}_{\text{sph}}$ and $\mathbf{S}_{\text{dis}}$, which are modeled using hyperelasticity to account for energy stored in existing constituents due to load-induced deformations, $\mathbf{S}_{\text{act}}$ results from a metabolic process whereby contractile smooth muscle generates force and motion via oxidation of ATP. This active stress therefore does not result from 'strain energy' despite the ability to model it using an 'energy potential.' Here, we assume that the active portion of the Cauchy stress generated by a cohort of smooth muscle in the current configuration is

$$\widehat{\sigma}_{\text{act}}(s,\tau)=f_{\text{act}}(s)\,\mathbf{u}^{\text{m}}(s,\tau)\otimes\mathbf{u}^{\text{m}}(s,\tau), \quad (40)$$

where $f_{\text{act}}(s)$ is a scalar function, having units kPa, defined in the current configuration along the direction of the unit vector $\mathbf{u}^{\text{m}}(s,\tau)$ of an active muscle 'fiber' that was deposited at time $\tau$, where

$$\mathbf{u}^{\text{m}}(s,\tau)=\frac{\mathbf{F}(s)\,\mathbf{F}^{-1}(\tau)\,\mathbf{m}^{\text{m}}(\tau)}{\|\mathbf{F}(s)\,\mathbf{F}^{-1}(\tau)\,\mathbf{m}^{\text{m}}(\tau)\|}. \quad (41)$$

The associated current stretch ratio of an active muscle fiber, relative to its *in vivo* configuration at its time of deposition, is

$$\lambda^{\text{act}}(s,\tau)=\|\mathbf{F}(s)\,\mathbf{F}^{-1}(\tau)\,\mathbf{m}^{\text{m}}(\tau)\|. \quad (42)$$

For sufficiently long time scales (~ days to weeks), the actomyosin filament overlap is expected to readjust to optimize the force-length response (Bai *et al.*, 2004; Langille *et al.*, 1989). Hence, $f_{\text{act}}(s)$ can be assumed to not be a function of $\mathbf{C}(s)$, but rather (Valentín *et al.*, 2011)

$$f_{\text{act}}(s)=\frac{\rho^{\text{m}}(s)}{\rho(s)}\,T_{\max}\{1-\exp\left(-C^2(s)\right)\}, \quad (43)$$

where $\rho^{\text{m}}(s)$ is the evolving mass density of smooth muscle, $T_{\max}$ is the maximum stress generated by smooth muscle, and

$$C(s)=C_{\text{b}}-C_{\text{s}}\,\Delta\tau_{\text{w}}(s) \quad (44)$$

is the ratio of vasoconstrictors to vasodilators; $C_{\text{b}}$ is a basal ratio, $C_{\text{s}}$ is a factor which scales the effect of changes in flow-induced luminal shear stress $\Delta\tau_{\text{w}}(s)=\tau_{\text{w}}(s)/\tau_{\text{w}}^{\text{h}}-1$ where $\tau_{\text{w}}(s)$ and $\tau_{\text{w}}^{\text{h}}$ are the current and homeostatic shear stresses, respectively. The cohort-specific active contribution to the second Piola-Kirchhoff stress tensor (for details see Appendix 3) is thus

$$\widehat{\mathbf{S}}_{\text{act}}(s,\tau)=\frac{f_{\text{act}}(s)\,J(s)}{I_4^{\text{act}}(s,\tau)}\mathbf{A}(\tau), \quad (45)$$

where

$$I_4^{\text{act}}(s,\tau)=\mathbf{F}^{-1}(\tau)\,\mathbf{m}^{\text{m}}(\tau)\cdot\mathbf{C}(s)\,\mathbf{F}^{-1}(\tau)\,\mathbf{m}^{\text{m}}(\tau), \quad \mathbf{A}(\tau)=\mathbf{F}^{-1}(\tau)\,\mathbf{m}^{\text{m}}(\tau)\otimes\mathbf{F}^{-1}(\tau)\,\mathbf{m}^{\text{m}}(\tau), \quad (46)$$

and $I_4^{\text{act}}(s,\tau)=\lambda^{\text{act}}(s,\tau)^2$. Finally, the contribution to the stiffness tensor by a cohort of active smooth muscle (for details see Appendix 4) is

$$\widehat{\mathbb{C}}_{\text{act}}(s,\tau)=2\frac{\partial\widehat{\mathbf{S}}_{\text{act}}(s,\tau)}{\partial\mathbf{C}(s)}=\widehat{\mathbf{S}}_{\text{act}}(s,\tau)\otimes\left(\mathbf{C}^{-1}(s)-\frac{2}{I_4^{\text{act}}(s,\tau)}\mathbf{A}(\tau)\right). \quad (47)$$

**2.3.5 Evolving mass density production—**Functional elastin is thought to be produced primarily during the perinatal period, hence we let $m^e(\tau)\equiv 0$. Conversely, we prescribe non-negative piecewise functions for stress-mediated rates of mass density production for smooth muscle and collagen (cf., Baek *et al.*, 2005, 2006; Valentín *et al.*, 2011)

$$m^\alpha(\tau)=m_0^\alpha\{\Upsilon(K_\sigma^\alpha,\delta_\sigma^\alpha)+\Upsilon(K_{\tau_w}^\alpha,\delta_{\tau_w}^\alpha)\}/2, \quad (48)$$

where $m_0^\alpha=\rho^\alpha(0)\,K_{q_h}^\alpha$ are basal rates of mass density production, $K_0^\alpha$ and $K_{\tau_w}^\alpha$ are rate parameters that govern constituent level stress- and wall shear stress-driven mass production, respectively, $\delta_\sigma^\alpha=\Delta\sigma^\alpha(\tau)$ and $\delta_{\tau_w}^\alpha=-(C_s/C_b)\,\Delta\tau_w(\tau)$ (see table 1 for parameter values). The quantity $\Delta\sigma^\alpha(\tau)=\sigma^\alpha(\tau)/\sigma^\alpha(0)-1$ is a scalar measure of the change in the distortional stress borne by each constituent family where

$$\sigma^\alpha(\tau)=\|\sigma_{\text{dis}}^\alpha(\tau)\,\mathbf{m}^\alpha(\tau)\|, \quad (49)$$

and $\mathbf{m}^\alpha(\tau)$ depends on the local mechanical environment at the time of deposition (see §2.3.7). For smooth muscle, we include both passive and active contributions to the growth stimulus via $\sigma^m(\tau)=\|(\sigma_{\text{dis}}^m(\tau)+\sigma_{\text{act}}(\tau))\,\mathbf{m}^m(\tau)\|$.

The mass production rate scaling function $\Upsilon(\cdot)$ is

$$\Upsilon(K_{(\cdot)}^\alpha,\delta_{(\cdot)}^\alpha)=\begin{cases}0 & \forall\delta_{(\cdot)}^\alpha\in(-\infty,l_{\text{neg}}),\\ \frac{1}{2}\left[1+\sin\left(\omega_{\text{neg}}\left\{\delta_{(\cdot)}^\alpha+b_{\text{neg}}\right\}\right)\right] & \forall\delta_{(\cdot)}^\alpha\in[l_{\text{neg}},0),\\ \frac{1}{2}\left[\{m_{\max}^\alpha+1\}+\{m_{\max}^\alpha-1\}\sin\left(\omega_{\text{pos}}\left\{\delta_{(\cdot)}^\alpha-b_{\text{pos}}\right\}\right)\right] & \forall\delta_{(\cdot)}^\alpha\in[0,l_{\text{pos}}),\\ m_{\max}^\alpha & \forall\delta_{(\cdot)}^\alpha\in[l_{\text{pos}},\infty),\end{cases} \quad (50)$$

where $m_{\max}^\alpha$ are maximal (limiting) values for mass density productions. Parameters $\omega_{\text{neg}}=2\,K_{(\cdot)}^\alpha$ and $\omega_{\text{pos}}=2\,K_{(\cdot)}^\alpha/(m_{\max}^\alpha-1)$ govern the period of the sinusoidal functions; $b_{\text{neg}}=\pi/(2\,\omega_{\text{neg}})$ and $b_{\text{pos}}=\pi/(2\,\omega_{\text{pos}})$ provide appropriate offsets; and $l_{\text{neg}}=-\pi/\omega_{\text{neg}}$ and $l_{\text{pos}}=\pi/\omega_{\text{pos}}$ define saturation limits (see figure 2). Equations (48) and (50) recover basal rates of production for $\delta_{(\cdot)}^\alpha=0$, as desired. This phenomenological functional form, which elaborates on the concept first proposed by Fung (1990, pg. 530), preserves the feature whereby parameters $K_{(\cdot)}^\alpha$ correspond to the maximum slope of $\Upsilon(\cdot)$ and approximates two hypothesized behaviors: saturation as mechanobiological stimuli approach limiting values and a nearly constant basal mass production rate near the homeostatic chemomechanical state.

**2.3.6 Evolving survival fractions—**The survival fraction of originally existing constituent $\alpha$ is (Valentín *et al.*, 2009)

$$Q^\alpha(s)=\exp\left(-\int_0^s\widehat{K}_q^\alpha(\tilde{\tau})\,\mathrm{d}\tilde{\tau}\right), \quad (51)$$

where $\widehat{K}_q^\alpha(s)=K_{q_\mathrm{h}}^\alpha\left(1+\Delta\widehat{\zeta}^\alpha(s)^2\right)$ are evolving cohort-specific rate-type parameters for mass removal with units of days$^{-1}$, and $K_{q_\mathrm{h}}^\alpha$ is the homeostatic constant of decay for both fibrillar collagen and smooth muscle, corresponding to a half-life of 70 days (see table 1). Thus, we model collagen and smooth muscle degradation as functions of cumulative changes of cohort-specific levels of tension, with

$$\Delta\widehat{\zeta}^\alpha(s)=\left(\frac{\partial\widehat{W}^\alpha}{\partial\lambda_\mathrm{n}^\alpha}\left(\lambda_{\mathrm{n}(\tau)}^\alpha(s)\right)/\frac{\partial\widehat{W}^\alpha}{\partial\lambda_\mathrm{n}^\alpha}(G_\mathrm{h}^\alpha)\right)-1 \quad (52)$$

being the normalized difference between fiber tensions at times $s$ and deposition time $\tau$ within an individual cohort of constituent $\alpha$. The above relations reflect the hypothesis that increases and decreases in fiber tension away from a homeostatic value, which in our model is greater than zero, will accelerate fiber degradation, consistent with diverse observations (Bendeck *et al.*, 2000; Galis *et al.*, 2002; O'Callaghan and Williams, 2000; Strauss *et al.*, 1996). Moreover, Camp *et al.* (2011) and Ruberti and Hallab (2005) reported that loaded collagen fibers experience reduced rates of enzymatic degradation, consistent with the notion that there exists a 'preferred' homeostatic stretch and corresponding load at which collagen degradation is most effectively inhibited. Generalizing equation (51) to permit the tracking of surviving fractions of subsequently produced cohorts yields

$$q^\alpha(s,\tau)=\exp\left(-\int_\tau^s\widehat{K}_q^\alpha(\tilde{\tau})\,\mathrm{d}\tilde{\tau}\right). \quad (53)$$

**2.3.7 Alignment of fibrillar constituents—**Recent observations reveal that the primary families of collagen fibers in the normal human aorta are found in constant radial planes and they tend to be oriented diagonally relative to the axial direction (Schriefl *et al.*, 2011). Nevertheless, because of a continuing lack of information on collagen cross-links, constitutive models including axial, circumferential, and symmetric diagonal fibers provide good fits to available biaxial data (Ferruzzi *et al.*, 2011). Hence, amongst the different hypotheses that could be examined, for illustrative purposes we assume that cells orient newly-deposited collagen so that $\mathbf{m}^{k=1}(\tau)=\hat{\mathbf{n}}_1(\tau)$ and $\mathbf{m}^{k=2}(\tau)=\hat{\mathbf{n}}_2(\tau)$, where $\hat{\mathbf{n}}_1(\tau)$ and $\hat{\mathbf{n}}_2(\tau)$ are the first and second principal directions (eigenvectors), respectively, of the deviatoric part of the Cauchy stress tensor $\boldsymbol{\sigma}_{\mathrm{dev}}(\tau)$ at the time of deposition (cf., Baek *et al.*, 2006; Driessen *et al.*, 2003; Hariton *et al.*, 2007). Given prescribed values for composition and constitutive parameters of the healthy artery (table 1), the first principal direction is the circumferential direction and the second is the axial direction; for the diagonal fibers, we similarly assume

$$\mathbf{m}^{k=3}(\tau)\cdot\mathbf{m}^{k=1}(\tau)=\frac{\sqrt{2}}{2},\quad \mathbf{m}^{k=3}(\tau)\cdot\mathbf{m}^{k=2}(\tau)=\frac{\sqrt{2}}{2},\quad \mathbf{m}^{k=3}(\tau)\cdot(\mathbf{m}^{k=1}(\tau)\times\mathbf{m}^{k=2}(\tau))=0, \quad (54)$$

and

$$\mathbf{m}^{k=4}(\tau)\cdot\mathbf{m}^{k=1}(\tau)=\frac{\sqrt{2}}{2},\quad \mathbf{m}^{k=4}(\tau)\cdot\mathbf{m}^{k=2}(\tau)=-\frac{\sqrt{2}}{2},\quad \mathbf{m}^{k=4}(\tau)\cdot\left(\mathbf{m}^{k=1}(\tau)\times\mathbf{m}^{k=2}(\tau)\right)=0, \quad (55)$$

which admit solutions for the directions of the remaining two families of collagen, where the operator × denotes the vector (cross) product. Smooth muscle is hypothesized to be deposited in the first principal direction $\mathbf{m}^{\mathrm{m}}(\tau)=\hat{\mathbf{n}}_1(\tau)$. Figure 3 shows the local orientations of fibers within our finite element model. This distribution will remain unchanged in the special case of tissue maintenance, as desired.

### 2.4 Numerical Implementation

Although both the G&R implementation and the numerical methods are general, we now describe a simplified geometry and set of boundary conditions to reduce the problem to a case that can be compared with prior semi-inverse analyses. We focus on a two-layered model of the human abdominal aorta and construct a quarter-symmetric mesh of single element in axial length. See table 1 for relevant geometric, kinetic, and other layer-specific quantities. Figure 3 shows our spatial domain and finite element discretization. Boundary conditions permit only radial nodal displacements, and we prescribe a pressure of $P = 93$ mmHg over the luminal surface. This boundary-value problem reduces to a singledimensional analysis of the inflation of a thick-walled tube of fixed axial length. Our finite element formulation allows cases of increased axial extension and/or perivascular tethering (Humphrey and Na, 2002; Valentín and Humphrey, 2009c), but we restrict our treatment to a fixed axial length and neglect perivascular tethering to concentrate on verification of the constrained mixture framework.

This finite element model is implemented as a user-specified material within *FEAP* (Taylor, 2008), using a *Q1-P0* 'mixed' element, based on Hu and Washizu's three-field variational approach (Holzapfel, 2000; Holzapfel and Ogden, 2003; Wriggers, 2008). This element employs linear shape functions for deformations and is appropriate for modeling incompressible materials. Eigenvectors and corresponding eigenvalues are computed using *LAPACK* (Anderson *et al.*, 1999). All temporal integrations are performed using a trapezoidal rule quadrature with a constant temporal resolution of one week per time step. Results are calculated at Gauss points, and kinetic quantities are averaged over each element. Our mesh employs 882 8-noded hexahedral elements (1,900 nodes in total), and the boundary conditions result in a system with 1,900 degrees of freedom.

## 3 Special Cases for Verification

### 3.1 Homogenous Changes of Mass

We first examine predictions for the simplified case of uniformly changing constituent mass densities. That is, G&R is not permitted ($m^a \equiv 0$), and we prescribe $Q^a$ and thus $\rho^a$ directly, rather than by letting mass density evolve via equation (4). Furthermore, we require that smooth muscle activity be insensitive to changing inner radius by prescribing

$$f_{\text{act}}(s) = \frac{\rho^{\text{m}}}{\rho} T_{\max} \{1 - \exp(-C_{\text{b}}^2)\}. \quad (56)$$

Note that the ratio $\rho^{\text{m}}/\rho$ remains constant; the local mass densities of all constituents are prescribed to vary by the same proportion $J = \rho/\rho_0$.

For this case of homogeneous $J$ and a cylindrical geometry with fixed axial length, the current radial position is

$$r(J) = [J\{r^2(J_0) - r_{\text{i}}^2(J_0)\} + r_{\text{i}}^2(J)]^{1/2}, \quad (57)$$

where $r_{\text{i}}(J_0)$ is the original loaded inner radius, with $J_0 \equiv 1$, and $r_{\text{i}}(J)$ is the current loaded inner radius. The deformation gradient tensor for this motion, in matrix notation, is

$$[\mathbf{F}(J)]_{(r,\theta,z)} = \text{diag}\left[\frac{J\, r(J_0)}{r(J)}, \frac{r(J)}{r(J_0)}, 1\right]. \quad (58)$$

The global form of the radial equilibrium equation is (Humphrey, 2002; Ogden, 1984)

$$P=\int_{r_i}^{r_a}\frac{\sigma_{\theta\theta}-\sigma_{rr}}{r}\,\mathrm{d}r, \quad (59)$$

where $P$ is the transmural pressure, $r_a$ is the current adventitial radius, and $\sigma_{\theta\theta}$ and $\sigma_{rr}$ are the circumferential and radial components of the Cauchy stress, respectively. We compute the inner radius to satisfy equation (59) using the secant method, and spatial integration is performed using Gauss-Legendre quadrature.

### 3.2 Diffrential G&R

We adapt the semi-analytic approach described by Valentín *et al.* (2011) to serve as a benchmark against which to verify the present finite element model for the case of G&R driven by elastin degradation prescribed by

$$c^{\mathrm{e}}(s)=\varphi(s)\,c^{\mathrm{e}}(0), \quad (60)$$

where $\varphi(s) = \exp(-K^{\mathrm{e}} s)$ is an elastin integrity variable, and $c^{\mathrm{e}}(0)$ is the original shear modulus for elastin. This time-dependent perturbation drives local G&R processes described in §2.3.5, §2.3.6, and §2.3.7. The case of differential growth requires volumetric changes to be non-homogeneous (as the notation $J(r, s)$ explicitly states) in general, and the current radial position is

$$r(s)=\left(2\int_{r_i(0)}^{r(0)} r\,J(r,s)\,\mathrm{d}r+r_i^2(s)\right)^{1/2}, \quad (61)$$

where $r_i(0)$ is the loaded inner radius at G&R time $s = 0$, and $r_i(s)$ is the evolving loaded inner radius at current G&R time $s$. Similar to equation (58), our time-dependent deformation gradient tensor is

$$[\mathbf{F}(s)]_{(r,\theta,z)}=\mathrm{diag}\left[\frac{J(s)r(0)}{r(s)},\frac{r(s)}{r(0)},1\right]. \quad (62)$$

Flow-induced luminal shear stresses vary with the inner radius

$$\tau_w(s)=\frac{4\mu Q}{\pi r_i^3(s)}, \quad (63)$$

where $\mu$ is the viscosity of whole blood and $Q$ is its constant volumetric flowrate. This relation drives both the vasoactive response and the shear-mediated rate of mass production via equations (43), (44), and (48). To capture the effects of local G&R, we track local kinetics at 251 equally-spaced points through the wall thickness and linearly interpolate kinetic quantities between them. This level of discretization provides high spatial resolution appropriate for use as a benchmark. As in the case of uniform changes of mass, we solve for $r_i(s)$ by satisfying equation (59).

## 4 Results

### 4.1 Homogenous Changes of Mass

Figure 4 shows the inner radius as a function of the homogenous volume ratio $J$. These results show, perhaps counterintuitively, that as individually prestretched constituents within

an inflated and axially fixed artery were lost, the inner radius tended to decrease. This phenomenon can be understood by recalling the global form for radial equilibrium equation (59) and that Cauchy stress is inversely proportional to $J$. For a given inner radius, $\lim_{J\to 0} \sigma_{\theta\theta}=\infty$, and a greater transmural pressure will be required to maintain a constant inner radius. For $P$ constant, however, $\sigma_{\theta\theta}$ and $\theta_{rr}$ experienced modest changes (figure 5), and the inner radius had to decrease to satisfy radial equilibrium. Note that this situation is unlike the familiar instance of a pressurized vessel with a decreasing fraction of mechanically effective material that remains in the wall ($J \equiv 1$), for which the inner radius increases.

Figure 4 also reveals the important influence of the adaptive penalty function described by equation (20). As $J \to 0$, the numerical problem became more demanding, and a higher penalty was required to converge to the correct solution. With greater $\beta$, the penalty function permitted the model to converge to better solutions. Our simulated artery revealed that this numerical obstacle became difficult to overcome for losses of mass in excess of 20%. No such limitation existed for increasing masses, however.

Cauchy stresses changed appreciably as the artery lost mass uniformly. Figure 5 shows transmural distributions of circumferential and axial stress as mass was removed numerically. The circumferential Cauchy stresses changed modestly, especially within the adventitia, but axial stresses changed far more appreciably. As a result of the fixed axial length and decreasing $J$, axial stresses increased as mass was removed. This increase in axial stress was particularly dramatic in the adventitia, where the higher percentage of exponentially stiff collagen carried a disproportionally higher load than the more compliant (and less abundant) elastin. This striking result is not necessarily physiologically relevant, but it reveals numerically important trends in this limiting case of prescribed uniform mass loss.

Figure 6 shows deviatoric stresses in circumferential and axial directions, which changed with varying $J$ but were nearly constant within each layer. These trends also reveal why the finite element model benefitted from a higher penalty parameter $K(J)$. As $J \to 0$, the deviatoric contributions became far greater than the spherical contributions. Because $K(J)$ penalizes the solution through the spherical portion of the stresses via equations (7) and (19), a greater value of $K(J)$ was required to maintain a constant overall penalizing effect.

The case of a uniform gain of mass was far less demanding numerically. Figure 7 shows that the circumferential Cauchy stresses in the media and axial stresses in both layers decreased with increasing $J$, as expected by recalling that $\boldsymbol{\sigma}$ and $J$ are inversely related and that the axial length of the artery was fixed. The finite element model matched the semi-analytic solution, even for a uniform twofold increase in mass. As in the case of mass loss, figure 8 predicted nearly constant transmural distributions of deviatoric stresses, though the trends of an increasing circumferential component and a decreasing axial component were opposite the case of mass loss, as expected. In fact, the axial deviatoric stresses became compressive in both the media and adventitia.

### 4.2 Differential G&R

Figure 9 shows the evolving geometry over 24 months as elastin degraded for varying values of $C_s$. The artery was predicted to distend and become thinner as a result of G&R. As $\varphi(s)$ decreased, the passive contribution by elastin diminished, and the artery distended. This expanding trend stretched existing circumferentially- and helically-aligned families of fibrillar constituents and accelerated removal via equations (51) to (53). Figure 10 reveals the evolving local gradients of volumetric changes (computed per a unit reference) as a result of locally-evolving mass removal and production rates. The finite element model

agreed well with the semi-analytic model, though some predictions diverged modestly with increasing G&R time.

Mass density production rates depend on local mechanical conditions and the luminal shear stress-driven constrictor concentration (herein assumed to have achieved a steady-state and thus uniformly diffused). Figure 11 shows that gradients began to appear in mass density production rates for circumferential and less so helical collagen by six months. Despite the elevated rates of production, due to the complementary effects of increasing intramural stresses and decreasing luminal wall shear stress (and thus increasing constrictor concentration), local volumes continued to decrease, indicating that removal outpaced replacement, particularly toward the luminal side of the artery. Results from the finite element model differed more from those from the semi-analytic result as G&R time progressed.

Production of medial smooth muscle (figure 12, panel a) and adventitial axial collagen (panel b) did not exhibit the aforementioned gradients, likely because the driving chemomechanical metrics were more uniform for these two constituents. The production rate of smooth muscle depended upon its distortional stress borne and active stress generated. Because the active stress depended on the chemical constrictor to dilator ratio $C(s)$, which on the timescales considered here was assumed to be uniformly diffused throughout the media, the active stress was spatially uniform. This effect tended to flatten the production rate distribution for smooth muscle. Production rates of axially-aligned adventitial collagen depended, in large part, on the distortional stress in the axial direction, which due to the fixed axial length remained nearly constant for all G&R times considered.

The circumferential and axial Cauchy stresses changed only modestly (figure 13), and the finite element model predicted close agreement with the semi-analytic model (figure 14). These models recovered the tendency that axial stress decreased and the unloaded axial length increased as elastin degraded, consistent with observations in the literature and previous analyses (Del Corso *et al.*, 1998; Fonck *et al.*, 2007; Jackson *et al.*, 2002, 2005; Wenn and Newman, 1990). The deviatoric stresses (figure 15), which determine the orientations of newly-deposited fibers, are perhaps more important. Again, the finite element model closely matched predictions from the semi-analytic model (figure 16), though agreement diverged beyond six months. The near constant transmural distributions of deviatoric stresses are of note, though this was expected since the deviatoric stresses were, in large part, the driving mechanical stimuli for G&R with the model essentially requiring synthesizing cells to work to maintain or approach homeostatic conditions. Although irreversible damage to elastin precludes an artery from maintaining its homeostatic geometry and composition, the evolving suboptimal state demonstrated that the artery can remain functional.

## 5 Discussion

We implemented an extended constrained mixture model of aortic G&R within a 3-D finite element framework. This flexible and powerful tool applies the concepts of the constrained mixture theory, in their most general forms to date, and accounts for locally evolving masses and orientations of individual constituents as functions of chemical and mechanical stimuli. The formulation posits that constituent-specific distortional stresses (which are assumed to be uniform within each layer in homeostasis but may change as the artery evolves in response to perturbations or disease) drive the rates of mass density production. This simple assumption permits the model to recover expected behavior in homeostasis (i.e., constant rates of mass production independent of location within a given arterial layer) and allows for differential G&R to occur as a function of 3-D field quantities, rather than mean intramural

stress. In addition, we exploited the availability of well-understood semi-inverse solutions for special cases to verify the correctness of this finite element implementation (Anderson *et al.*, 2007). The simple, yet useful and physiologically-relevant, geometry and boundary conditions for the extension and inflation of a thick-walled tube allowed a conceptually broad treatment by including key G&R postulates: that synthesizing cells deposit new material under a state of prestretch, that the rate of turnover of material varies in response to the local chemomechanical environment, and that smooth muscle can generate stress actively in response to changing flow-induced chemical signals (Valentín and Holzapfel, 2012; Valentín and Humphrey, 2009a). The orientations of newly-deposited fibers are assumed to depend upon the eigenvectors of the deviatoric stress, which, for the cases of G&R presented, remained constant.

The requirement of allowing large changes in mass (and volume) due to G&R while enforcing isochoric responses to transients in loading necessitated a novel extension of traditional finite strain finite element formulations. The traditional penalty parameter was extended to a function. Our current choice for the functional form for $K(J)$ in equation (20) is an *ad hoc* attempt to improve convergence for the (unrealistically) large degrees of mass loss without turnover, which resulted in the marked increases in axial deviatoric stresses seen in figure 6. Nonetheless, in all cases of uniform changes of mass for this geometry and set of boundary conditions, the finite element model captured well all the trends predicted by the semi-analytic model. In fact, the finite element results were nearly identical to the semi-analytic solution for $J \in [0.85, 2.0]$, and only began to deviate once $J$ decreased further. It thus appears that the finite element model is suitable for simulating physiologically-relevant conditions.

The modest discrepancies seen between the finite element and semi-analytic models of differential G&R can be attributed, in part, to mass kinetics being constant within each element. Given the limited spatial resolution of the finite element compared to the semi-analytic model (18 elements versus 250 interpolation subdomains points, respectively, for tracking mass kinetics in the radial dimension), it should not be surprising that the solutions will tend to diverge with increasing G&R time as a result of accumulating error via the convolution integral of historical mass kinetics.

In traditional finite element analyses in solid mechanics using an unstressed ‘ground state’ as the reference configuration, increased spatial resolution via appropriate mesh refinement results in convergence towards the ‘true’ solution. For a given set of mechanical parameters and boundary and initial conditions, our model exhibits the same convergence with increased spatial resolution (not shown). In this model, however, it is convenient to use a loaded and stressed configuration as a reference, and this reference state must be fully mechanically characterized *a priori*. That is, we must know the constitutive behavior that recovers a desired geometry for a given set of tractions. So as not to overpresecribe the problem, we specify all mechanical parameters, save one, which we allow to be ‘free’ and solve it such that our model recovers a desired homeostatic geometry at a known transmural pressure. In our case, this ‘free’ variable is $c_2^k$; is computed using the semi-analytic model in an inverse manner.

In our G&R problem, we must also identify the homeostatic scalar metrics of stress (see equation (49)) that drive mass production rates. Similar to the free parameter described above, these scalar stresses come from our semi-analytic model and recover G&R homeostasis, maintaining the desired geometry and mechanical properties at normal physiological loads. Ideally, once those quantities are substituted into the finite element model and the boundary conditions imposed, the finite element model will precisely recover the desired homeostatic, reference geometry. Yet error arising from discretization results in

slight deviations from the desired loaded geometry, resulting in an effectively different set of initial conditions for our time-dependent G&R simulation. These differences, though initially small, manifest as compounding errors in the kinetics when compared to our benchmark semi-analytic model.

This source of error in the finite element model does not affect the solutions for the case of uniform mass kinetics; there is no accumulation of error or any need to resolve the local effects of G&R. Some important pathologies, such as vasospasm, progress and resolve over multiple distinct phases, each possessing their own characteristic timescales (Baek *et al.*, 2007; Humphrey *et al.*, 2007). Although the computational cases presented utilize constant temporal resolutions, we speculate that simulations for more complex cases of arterial G&R will benefit from variable temporal resolutions. Our assumption of a motion-independent active force function $f_{\text{act}}(s)$ (see equation (43)) would also need to be revisited for cases of G&R which occur over timescales of hours to days; evolving actomyosin filament overlap would need to be accounted for within the active response function (cf. Baek *et al.*, 2007; Valentín *et al.*, 2009).

Our 'integral-based' approach differs from the 'rate-based' approach introduced by Watton *et al.* (2004) in that we explicitly account for the history of G&R by tracking kinetics and motions over a finite timespan via equations (1) and (4). One advantage of our approach is the ability to account for time-varying mass production and degradation rates while retaining their biological interpretations. Nevertheless, the 'integral-based' formulation requires storing the history interval or interest in memory and performing an associated numerical integration. This is in contrast to the more computationally expedient 'rate-based' approach, as implemented in 3-D finite elements by Schmid *et al.* (2010) and Schmid *et al.* (2013), which does not track the motions and kinetics of individual cohorts of material. As a result of our more demanding computational problem, we confronted several numerical challenges in achieving numerical stability while balancing accuracy and computational expense. Chief among them is the management of computational requirements for storing histories of kinetics and motions. We can appreciate this matter by considering the related questions of temporal resolution and the necessarily finite timespan for tracking cohort-specific histories. For the case of differential G&R, a convergence analysis (not shown) demonstrated numerical stability and quadratic convergence with increasing temporal resolution, as desired. However, unlike typical elastodynamic problems where increased temporal resolution requires more time steps, our constrained-mixture G&R problem additionally requires a corresponding increase in the number of discrete cohorts to track. That is, increased temporal resolution requires not only more time steps, but also more memory use; this increased number of cohorts incurs additional CPU expense in numerically evaluating the various integral relations. Our analysis revealed that for the present axisymmetric problem, regardless of temporal resolution, it is necessary to track for a minimum of 10 half-lives of collagen to ensure numerical stability.

We assumed that newly-deposited fibers are aligned relative to directions of principal deviatoric stress. In the cases considered, the orientations of fiber families remained constant, though their relative quantities changed. Naturally, these directions need not be constant in the general case of non-axisymmetric motions or boundary conditions, as in irregularly-shaped aneurysms. That is, the eigenvectors of the deviatoric stress tensor should change with complex motions and states of stress (e.g., the emergence of shear stresses), resulting in each cohort of fibrillar material being oriented uniquely; co-existing fiber cohorts will move together within the constrained mixture, but their collective orientations will constitute a distribution. Indeed, even for axisymmetric motions, the first and second principal directions in the adventitia will switch if axial stresses evolve to exceed circumferential stresses. Of course, the nature of the mechanical stimuli dictating fiber

alignment remains an open question. However, eigenvectors of stress are reasonable first guesses, and regardless of which metric is chosen, it will be necessary to identify, characterize, and address any associated numerical challenges. Finally, we speculate that it is possible that penalty functions explicitly accounting for the ratio of spherical to deviatoric stresses would yield better results for numerically demanding conditions such as instances of substantial losses of mass. Each of these aforementioned topics warrants careful consideration for specific boundary-value problems and more in-depth study, in general.

The present framework addresses the need pointed out by Humphrey and Holzapfel (2012) for more general tools for analyzing complex boundary value problems involving patient-specific geometries and the progression of vascular diseases. The pressing need for improved models that can account for more diverse conditions has prompted broader theoretical treatments to address myriad aspects and complexities of general differential growth. Consistent with the overarching goal of investigating and modeling the evolving structural and functional properties of soft tissues as multiscale phenomena via numerical experiments, computational models continue to achieve refinements in hypothesized driving mechanisms for G&R and homeostasis (i.e., the chemomechanical quantities that drive the rates of turnover and alignments of newly synthesized collagen). By extending the core theoretical framework to account for less idealized scenarios, we can better investigate G&R as a process which arises naturally from changes in microstructure.

## Acknowledgments

This work was supported, in part, by NIH grant HL-086418 via the program, Collaborations with National Centers for Biomedical Computing (SimBios at Stanford University) and NIH grant HL-105297. We acknowledge thoughtful discussions with and technical assistance from T. S. E. Eriksson, Ph.D.

## Appendix 1

We can show equation $(25)_2$ by using the product rule to obtain

$$\frac{\partial \overline{I_1^{\mathrm{e}}}(s)}{\partial \mathbf{C}(s)} = \frac{\partial}{\partial \mathbf{C}(s)} \operatorname{tr}\left(J^{-2/3}(s)\,\mathbf{C}^{\mathrm{e}}(s)\right) = \frac{\partial J^{-2/3}(s)}{\partial \mathbf{C}(s)} \operatorname{tr}\mathbf{C}^{\mathrm{e}}(s) + J^{-2/3}(s)\,\frac{\partial \operatorname{tr}\mathbf{C}^{\mathrm{e}}(s)}{\partial \mathbf{C}(s)}. \quad \text{(A.1)}$$

We then use the chain rule to write

$$\frac{\partial J^{-2/3}(s)}{\partial \mathbf{C}(s)} = \frac{\partial J^{-2/3}(s)}{\partial J(s)} \frac{\partial J(s)}{\partial I_3(s)} \frac{\partial I_3(s)}{\partial \mathbf{C}(s)}, \quad \text{(A.2)}$$

where $I_3(s) = \det \mathbf{C}(s) = J^2(s)$. Recalling the relation $\partial I_3(s)/\partial \mathbf{C}(s) = I_3(s)\,\mathbf{C}^{-1}(s)$, we may rewrite equation (A.2) as

$$\frac{\partial J^{-2/3}(s)}{\partial \mathbf{C}(s)} = -\frac{2}{3} J^{-5/3}(s) \frac{1}{2} J^{-1}(s)\; J^2(s)\,\mathbf{C}^{-1}(s) = -\frac{1}{3} J^{-2/3}(s)\;\mathbf{C}^{-1}(s). \quad \text{(A.3)}$$

Turning our attention to the second term of equation $(A.1)_2$ we note that $\mathbf{C}^{\mathrm{e}}(s) = (\tilde{\mathbf{G}}^{\mathrm{e}})^{\mathrm{T}}\,\mathbf{C}(s)\,\tilde{\mathbf{G}}^{\mathrm{e}}$ and that

$$\operatorname{tr}\left(\left(\tilde{\mathbf{G}}^{\mathrm{e}}\right)^{\mathrm{T}} \mathbf{C}(s)\,\tilde{\mathbf{G}}^{\mathrm{e}}\right) = \operatorname{tr}\left(\tilde{\mathbf{G}}^{\mathrm{e}}\left(\tilde{\mathbf{G}}^{\mathrm{e}}\right)^{\mathrm{T}} \mathbf{C}(s)\right). \quad \text{(A.4)}$$

Letting $\mathbf{G} = \tilde{\mathbf{G}}^{\mathrm{e}} (\tilde{\mathbf{G}}^{\mathrm{e}})^{\mathrm{T}}$ and recalling that $\mathbf{C}(s)$: $\mathbf{G}$ = tr ($\mathbf{G}\,\mathbf{C}^{\mathrm{T}}(s)$), where $\mathbf{C}(s) = \mathbf{C}^{\mathrm{T}}(s)$, we can write

$$\mathrm{tr}\left(\tilde{\mathbf{G}}^{\mathrm{e}}\left(\tilde{\mathbf{G}}^{\mathrm{e}}\right)^{\mathrm{T}}\mathbf{C}(s)\right)=\mathbf{C}(s):\mathbf{G}. \quad \text{(A.5)}$$

The partial derivative with respect to the current right Cauchy-Green tensor is

$$\frac{\partial\left(\mathbf{C}(s):\mathfrak{G}\right)}{\partial\mathbf{C}(s)}=\mathbf{C}(s):\frac{\partial\mathfrak{G}}{\partial\mathbf{C}(s)}+\mathfrak{G}:\frac{\partial\mathbf{C}(s)}{\partial\mathbf{C}(s)}=\mathfrak{G}=\tilde{\mathbf{G}}^{\mathrm{e}}\left(\tilde{\mathbf{G}}^{\mathrm{e}}\right)^{\mathrm{T}}. \quad \text{(A.6)}$$

Finally, using equations $(A.3)_2$ and $(A.6)_3$ yields the desired result.

## Appendix 2

To derive equation (35), we recall equation $(31)_2$. By using the product rule, recalling equation $(A.3)_2$, and noting that

$$\frac{\partial}{\partial\mathbf{C}(s)}\left\{\overline{\eta^{\alpha}}(\tau)\cdot\mathbf{C}(s)\,\overline{\eta^{\alpha}}(\tau)\right\}=\overline{\eta^{\alpha}}(\tau)\otimes\overline{\eta^{\alpha}}(\tau), \quad \text{(A.7)}$$

we obtain

$$\frac{\partial\overline{I^{\alpha}_{4_{\mathrm{n}(\tau)}}}(s)}{\partial\mathbf{C}(s)}=-\frac{1}{3}\left\{\overline{\eta^{\alpha}}(\tau)\cdot\mathbf{C}(s)\,\overline{\eta^{\alpha}}(\tau)\right\}J^{-2/3}(s)\,\mathbf{C}^{-1}(s)+J^{-2/3}(s)\,\overline{\eta^{\alpha}}(\tau)\otimes\overline{\eta^{\alpha}}(\tau). \quad \text{(A.8)}$$

Back-substitution of equation $(31)_2$ yields the desired result.

## Appendix 3

Here, we derive equation (45). Applying an inverse Piola transformation ('pulling back') to the actively generated contribution in the current configuration from equation (40) yields the corresponding contribution to the Piola-Kirchhoff stress

$$\widehat{\mathbf{S}}_{\mathrm{act}}(s,\tau)=J(s)\,\mathbf{F}^{-1}(s)\,\widehat{\sigma}_{\mathrm{act}}(s,\tau)\,\mathbf{F}^{-\mathrm{T}}(s). \quad \text{(A.9)}$$

By using equations (40) to (42), we can rewrite equation (A.9) as

$$\begin{aligned}\widehat{\mathbf{S}}_{\mathrm{act}}(s,\tau)&=\frac{f_{\mathrm{act}}(s)\,J(s)}{\lambda^{\mathrm{act}}(s,\tau)^2}\mathbf{F}^{-1}(s)\,\mathbf{F}(s)\,\mathbf{F}^{-1}(\tau)\,\mathbf{m}^{\mathrm{m}}(\tau)\otimes\mathbf{F}(s)\,\mathbf{F}^{-1}(\tau)\,\mathbf{m}^{\mathrm{m}}(\tau)\,\mathbf{F}^{-\mathrm{T}}(s),\\&=\frac{f_{\mathrm{act}}(s)\,J(s)}{\lambda^{\mathrm{act}}(s,\tau)^2}\mathbf{F}^{-1}(\tau)\,\mathbf{m}^{\mathrm{m}}(\tau)\otimes\left(\mathbf{F}^{-1}(\tau)\,\mathbf{m}^{\mathrm{m}}(\tau)\right)^{\mathrm{T}}\mathbf{F}^{\mathrm{T}}(s)\,\mathbf{F}^{-\mathrm{T}}(s),\\&=\frac{f_{\mathrm{act}}(s)\,J(s)}{\lambda^{\mathrm{act}}(s,\tau)^2}\mathbf{F}^{-1}(\tau)\,\mathbf{m}^{\mathrm{m}}(\tau)\otimes\mathbf{F}^{-1}(\tau)\,\mathbf{m}^{\mathrm{m}}(\tau).\end{aligned} \quad \text{(A.10)}$$

Hence, by recalling equation $(46)_2$ and by noting that (see equation $(46)_1$)

$$\begin{aligned}\lambda^{\mathrm{act}}(s,\tau)^2 &= \mathbf{F}(s)\,\mathbf{F}^{-1}(\tau)\,\mathbf{m}^{\mathrm{m}}(\tau)\cdot\mathbf{F}(s)\,\mathbf{F}^{-1}(\tau)\,\mathbf{m}^{\mathrm{m}}(\tau),\\ &= \left(\mathbf{F}^{-1}(\tau)\,\mathbf{m}^{\mathrm{m}}(\tau)\right)^{\mathrm{T}}\cdot\mathbf{F}^{\mathrm{T}}(s)\,\mathbf{F}(s)\,\mathbf{F}^{-1}(\tau)\,\mathbf{m}^{\mathrm{m}}(\tau), \quad \text{(A.11)}\\ &= \mathbf{F}^{-1}(\tau)\,\mathbf{m}^{\mathrm{m}}(\tau)\cdot\mathbf{C}(s)\,\mathbf{F}^{-1}(\tau)\,\mathbf{m}^{\mathrm{m}}(\tau)=I_4^{\mathrm{act}}(s,\tau),\end{aligned}$$

we can substitute into equation $(A.10)_3$ to obtain the desired result.

## Appendix 4

We can show equation $(47)_2$ by recalling equation (45) and the relation (Holzapfel, 2000, Ch. 1.7)

$$\frac{\partial(\Phi\mathbf{A})}{\partial\mathbf{C}}=\mathbf{A}\otimes\frac{\partial\Phi}{\partial\mathbf{C}}+\Phi\frac{\partial\mathbf{A}}{\partial\mathbf{C}}, \quad \text{(A.12)}$$

where $\Phi$ is a smooth scalar-valued function, and $\mathbf{A}$ is a smooth tensor-valued function. Using the definition from equation $(46)_2$ for tensor $\mathbf{A}$ and noting that $\mathbf{A}(\tau)$ is constant in $\mathbf{C}(s)$ yields

$$\frac{\partial\widehat{\mathbf{S}}_{\mathrm{act}}(s,\tau)}{\partial\mathbf{C}(s)}=\mathbf{A}(\tau)\otimes\frac{\partial}{\partial\mathbf{C}(s)}\left(\frac{f_{\mathrm{act}}(s)\,J(s)}{I_4^{\mathrm{act}}(s,\tau)}\right)+\frac{f_{\mathrm{act}}(s)\,J(s)}{I_4^{\mathrm{act}}(s,\tau)}\cancelto{0}{\frac{\partial\mathbf{A}(\tau)}{\partial\mathbf{C}(s)}}, \quad \text{(A.13)}$$

Using the product rule,

$$\frac{\partial}{\partial\mathbf{C}(s)}\left(\frac{f_{\mathrm{act}}(s)\;J(s)}{I_4^{\mathrm{act}}(s,\tau)}\right)=\frac{1}{I_4^{\mathrm{act}}(s,\tau)}\frac{\partial(f_{\mathrm{act}}(s)\;J(s))}{\partial\mathbf{C}(s)}+f_{\mathrm{act}}(s)\;J(s)\frac{\partial\left(I_4^{\mathrm{act}}(s,\tau)^{-1}\right)}{\partial\mathbf{C}(s)}, \quad \text{(A.14)}$$

where, by using the property $\partial J(s)/\partial\mathbf{C}(s) = (J(s)/2)\,\mathbf{C}^{-1}(s)$,

$$\frac{\partial(f_{\mathrm{act}}(s)\;J(s))}{\partial\mathbf{C}(s)}=\frac{f_{\mathrm{act}}(s)\;J(s)}{2}\mathbf{C}^{-1}(s), \quad \text{(A.15)}$$

and, by using equation $(A.11)_3$,

$$\frac{\partial\left(I_4^{\mathrm{act}}(s,\tau)^{-1}\right)}{\partial\mathbf{C}(s)}=\frac{\partial\left(I_4^{\mathrm{act}}(s,\tau)^{-1}\right)}{\partial I_4^{\mathrm{act}}(s,\tau)}\frac{\partial I_4^{\mathrm{act}}(s,\tau)}{\partial\mathbf{C}(s)}=-\frac{1}{I_4^{\mathrm{act}}(s,\tau)^2}\mathbf{A}(\tau). \quad \text{(A.16)}$$

Substituting equations (A.14) to (A.16) into equation (A.13) yields

$$\frac{\partial\widehat{\mathbf{S}}_{\mathrm{act}}(s,\tau)}{\partial\mathbf{C}(s)}=\mathbf{A}(\tau)\otimes\left(\frac{f_{\mathrm{act}}(s)\;J(s)}{2I_4^{\mathrm{act}}(s,\tau)}\mathbf{C}^{-1}(s)-\frac{f_{\mathrm{act}}(s)\;J(s)}{I_4^{\mathrm{act}}(s,\tau)^2}\mathbf{A}(\tau)\right), \quad \text{(A.17)}$$

which after simplification gives the desired result in equation $(47)_2$.

## References


Anderson AE, Ellis BJ, Weiss JA. Verification, validation and sensitivity studies in computational biomechanics. Comput Methods Biomech Biomed Engin. 2007; 10(3):171–84. [PubMed: 17558646]

Anderson, E.; Bai, Z.; Bischof, C.; Blackford, S.; Demmel, J.; Dongarra, J.; Du Croz, J.; Greenbaum, A.; Hammarling, S.; McKenney, A.; Sorensen, D. LAPACK Users' Guide. 3. Society for Industrial and Applied Mathematics; Philadelphia: 1999.

Baek S, Rajagopal KR, Humphrey JD. Competition between radial expansion and thickening in the enlargement of an intracranial saccular aneurysm. J Elasticity. 2005; 80(19):13–31.

Baek S, Rajagopal KR, Humphrey JD. A theoretical model of enlarging intracranial fusiform aneurysms. J Biomech Eng. 2006; 128(1):142–9. [PubMed: 16532628]

Baek S, Valentín A, Humphrey JD. Biochemomechanics of cerebral vasospasm and its resolution: II. constitutive relations and model simulations. Ann Biomed Eng. 2007; 35(9):1498–509. [PubMed: 17487585]

Bai TR, Bates JHT, Brusasco V, Camoretti-Mercado B, Chitano P, Deng LH, Dowell M, Fabry B, Ford LE, Fredberg JJ, Gerthoffer WT, Gilbert SH, Gunst SJ, Hai C, Halayko AJ, Hirst SJ, James AL, Janssen LJ, Jones KA, King GG, Lakser OJ, Lambert RK, Lauzon A, Lutchen KR, Maksym GN, Meiss RA, Mijailovich SM, Mitchell HW, Mitchell RW, Mitzner W, Murphy TM, Pare PD, Schellenberg RR, Seow CY, Sieck GC, Smith PG, Smolensky AV, Solway J, Stephens NL, Stewart AG, Tang DD, Wang L. On the terminology for describing the length-force relationship and its changes in airway smooth muscle. J Appl Physiol. 2004; 97(6):2029–34. [PubMed: 15531570]

Bendeck MP, Irvin C, Reidy M, Smith L, Mulholland D, Horton M, Giachelli CM. Smooth muscle cell matrix metalloproteinase production is stimulated via $\alpha_v\beta_3$ integrin. Arterioscler Thromb Vasc Biol. 2000; 20(6):1467–72. [PubMed: 10845859]

Camp RJ, Liles M, Beale J, Saeidi N, Flynn BP, Moore E, Murthy SK, Ruberti JW. Molecular mechanochemistry: Low force switch slows enzymatic cleavage of human type I collagen monomer. J Am Chem Soc. 2011; 133(11):4073–8. [PubMed: 21348512]

Cardamone L, Valentín A, Eberth JF, Humphrey JD. Origin of axial prestretch and residual stress in arteries. Biomech Model Mechanobiol. 2009; 8(6):431–46. [PubMed: 19123012]

Del Corso L, Moruzzo D, Conte B, Agelli M, Romanelli AM, Pastine F, Protti M, Pentimone F, Baggiani G. Tortuosity, kinking, and coiling of the carotid artery: expression of atherosclerosis or aging? Angiology. 1998; 49(5):361–71. [PubMed: 9591528]

Dorrington K, McCrum N. Elastin as a rubber. Biopolymers. 1977; 16(6):1201–22. [PubMed: 880350]

Driessen NJB, Peters GWM, Huyghe JM, Bouten CVC, Baaijens FPT. Remodelling of continuously distributed collagen fibres in soft connective tissues. J Biomech. 2003; 36(8):1151–8. [PubMed: 12831741]

Ferruzzi J, Vorp DA, Humphrey JD. On constitutive descriptors of the biaxial mechanical behaviour of human abdominal aorta and aneurysms. J R Soc Interface. 2011; 8(56):435–50. [PubMed: 20659928]

Flory PJ. Thermodynamic relations for high elastic materials. Trans Faraday Soc. 1961; 57:829–38.

Fonck E, Prod'hom G, Roy S, Augsburger L, Rüfenacht DA, Stergiopulos N. Effect of elastin degradation on carotid wall mechanics as assessed by a constituent-based biomechanical model. Am J Physiol Heart Circ Physiol. 2007; 292(6):H2754–63. [PubMed: 17237244]

Fung, YC. Biomechanics: Motion, Flow, Stress, and Growth. Springer-Verlag; New York: 1990.

Galis ZS, Johnson C, Godin D, Magid R, Shipley JM, Senior RM, Ivan E. Targeted disruption of the matrix metalloproteinase-9 gene impairs smooth muscle cell migration and geometrical arterial remodeling. Circ Res. 2002; 91(9):852–9. [PubMed: 12411401]

Hariton I, de Botton G, Gasser TC, Holzapfel GA. Stress-driven collagen fiber remodeling in arterial walls. Biomech Model Mechanobiol. 2007; 6(3):163–75. [PubMed: 16912884]

Holzapfel, GA. Nonlinear Solid Mechanics. A Continuum Approach for Engineering. John Wiley & Sons Ltd.; Chichester: 2000.

Holzapfel, GA.; Ogden, RW. Biomechanics of Soft Tissue in Cardiovascular Systems. Springer-Verlag; Vienna, New York: 2003.

Holzapfel GA, Weizsäcker HW. Biomechanical behavior of the arterial wall and its numerical characterization. Comput Biol and Med. 1998; 28(4):377–92. [PubMed: 9805198]

Holzapfel GA, Gasser TC, Ogden RW. A new constitutive framework for arterial wall mechanics and a comparative study of material models. J Elasticity. 2000; 61(1-3):1–48.

Humphrey, JD. Cardiovascular Solid Mechanics: Cells, Tissues, and Organs. Springer-Verlag; New York: 2002.

Humphrey JD, Holzapfel GA. Mechanics, mechanobiology, and modeling of human abdominal aorta and aneurysms. J Biomech. 2012; 45(5):805–84. [PubMed: 22189249]

Humphrey JD, Na S. Elastodynamics and arterial wall stress. Ann Biomed Eng. 2002; 30(4):509–23. [PubMed: 12086002]

Humphrey JD, Rajagopal KR. A constrained mixture model for growth and remodeling of soft tissues. Math Models Methods Appl Sci. 2002; 12(3):407–30.

Humphrey JD, Baek S, Niklason LE. Biochemomechanics of cerebral vasospasm and its resolution: I. a new hypothesis and theoretical framework. Ann Biomed Eng. 2007; 35(9):1485–97. [PubMed: 17487586]

Jackson ZS, Gotlieb AI, Langille BL. Wall tissue remodeling regulates longitudinal tension in arteries. Circ Res. 2002; 90(8):918–25. [PubMed: 11988494]

Jackson ZS, Dajnowiec D, Gotlieb AI, Langille BL. Partial off-loading of longitudinal tension induces arterial tortuosity. Arterioscler Thromb Vasc Biol. 2005; 25(5):957–62. [PubMed: 15746437]

Karšaj I, Sorić J, Humphrey J. A 3-D framework for arterial growth and remodeling in response to altered hemodynamics. Int J Engr Sci. 2010; 48:1357–72.

Langille BL, Bendeck MP, Keeley FW. Adaptations of carotid arteries of young and mature rabbits to reduced carotid blood flow. Am J Physiol. 1989; 256(4 Pt 2):H931–9. [PubMed: 2705563]

O'Callaghan CJ, Williams B. Mechanical strain-induced extracellular matrix production by human vascular smooth muscle cells: role of TGF-$\beta_1$. Hypertension. 2000; 36(3):319–24. [PubMed: 10988258]

Ogden, RW. Non-linear Elastic Deformations. John Wiley & Sons Ltd.; Chichester: 1984.

Ruberti JW, Hallab NJ. Strain-controlled enzymatic cleavage of collagen in loaded matrix. Biochem Biophys Res Commun. 2005; 336(2):483–9. [PubMed: 16140272]

Salsac A-V, Sparks SR, Lasheras JC. Hemodynamic changes occurring during the progressive enlargement of abdominal aortic aneurysms. Ann Vasc Surg. 2004; 18(1):14–21. [PubMed: 14712379]

Schmid H, Watton PN, Maurer MM, Wimmer J, Winkler P, Wang YK, Rohrle O, Itskov M. Impact of transmural heterogeneities on arterial adaptation: application to aneurysm formation. Biomech Model Mechanobiol. 2010; 9(3):295–315. [PubMed: 19943177]

Schmid H, Grytsan A, Poshtan E, Watton PN, Itskov M. Influence of differing material properties in media and adventitia on arterial adaptation–application to aneurysm formation and rupture. Comput Methods Biomech Biomed Engin. 2013; 16(1):33–53. [PubMed: 22149119]

Schriefl AJ, Zeindlinger G, Pierce DM, Regitnig P, Holzapfel GA. Determination of the layer-specific distributed collagen fibre orientations in human thoracic and abdominal aortas and common iliac arteries. J R Soc Interface. 2012; 9(71):1275–86. [PubMed: 22171063]

Strauss BH, Robinson R, Batchelor WB, Chisholm RJ, Ravi G, Natarajan MK, Logan RA, Mehta SR, Levy DE, Ezrin AM, Keeley FW. In vivo collagen turnover following experimental balloon angioplasty injury and the role of matrix metalloproteinases. Circ Res. 1996; 79(3):541–50. [PubMed: 8781487]

Taylor, RL. FEAP – A Finite Element Analysis Program, Version 8.2. University of California at Berkeley; 2008.

Valentín A, Holzapfel GA. Constrained mixture models as tools for testing competing hypotheses in arterial biomechanics: A brief survey. Mech Res Comm. 2012; 42:126–33.

Valentín A, Humphrey JD. Evaluation of fundamental hypotheses underlying constrained mixture models of arterial growth and remodelling. Phil Trans R Soc Lond A. 2009a; 367(1902):3585–606.

Valentín A, Humphrey JD. Parameter sensitivity study of a constrained mixture model of arterial growth and remodeling. J Biomech Eng. 2009b; 131(10):101006. [PubMed: 19831476]

Valentín A, Humphrey JD. Modeling effects of axial extension on arterial growth and remodeling. Med Biol Eng Comput. 2009c; 47(9):979–87. [PubMed: 19649667]

Valentín A, Cardamone L, Baek S, Humphrey JD. Complementary vasoactivity and matrix remodelling in arterial adaptations to altered flow and pressure. J R Soc Interface. 2009; 6(32): 293–306. [PubMed: 18647735]

Valentín A, Humphrey JD, Holzapfel GA. A multi-layered computational model of coupled elastin degradation, vasoactive dysfunction, and collagenous stiffening in aortic aging. Ann Biomed Eng. 2011; 39(7):2027–45. [PubMed: 21380570]

Vorp DA. Biomechanics of abdominal aortic aneurysm. J Biomech. 2007; 40(9):1887–902. [PubMed: 17254589]

Watton PN, Hill NA, Heil M. A mathematical model for the growth of the abdominal aortic aneurysm. Biomech Model Mechanobiol. 2004; 3(2):98–113. [PubMed: 15452732]

Wenn CM, Newman DL. Arterial tortuosity. Australas Phys Eng Sci Med. 1990; 13(2):67–70. [PubMed: 2375702]

Wriggers, P. Nonlinear Finite Element Methods. Springer-Verlag; Berlin, Heidelberg: 2008.

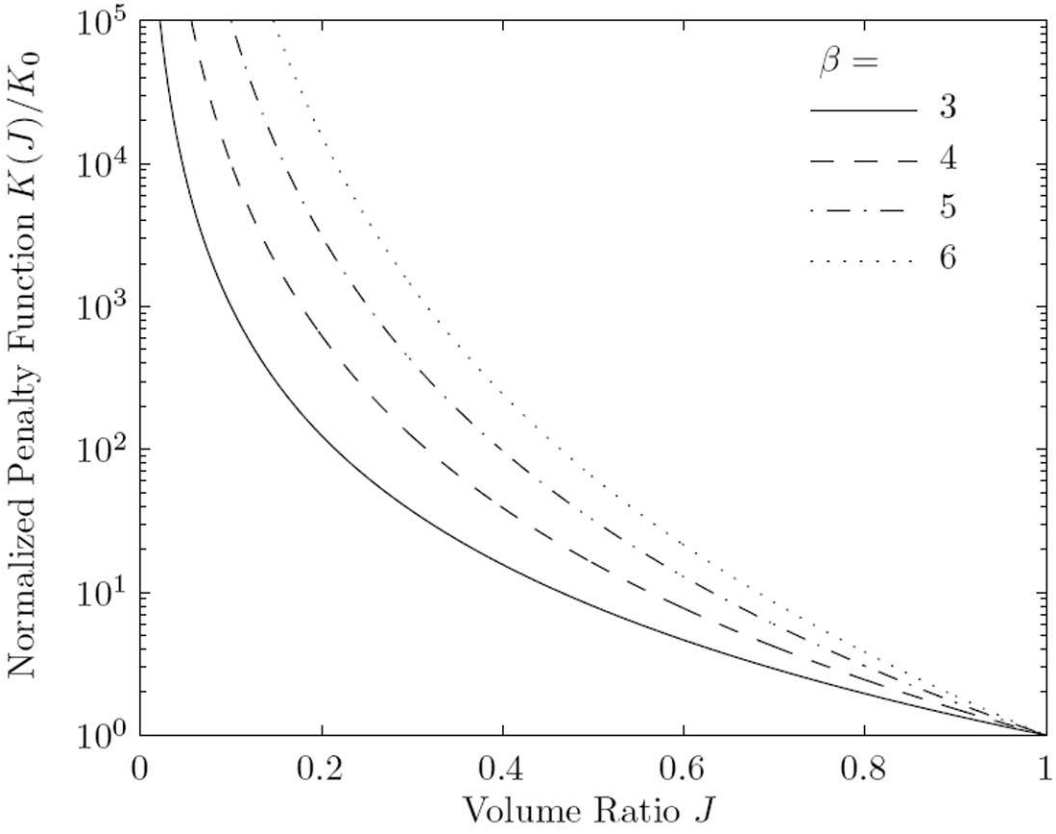


**Figure 1.**

Normalized penalty function $K(J)/K_0$, described in equation (20), on the interval $J \in (0, 1)$ for indicated values of $\beta$. This penalty function satisfies the requirement that $\lim_{J \to 0} K(J) = \infty$, which assists convergence for cases of large losses of mass, and thus volume.

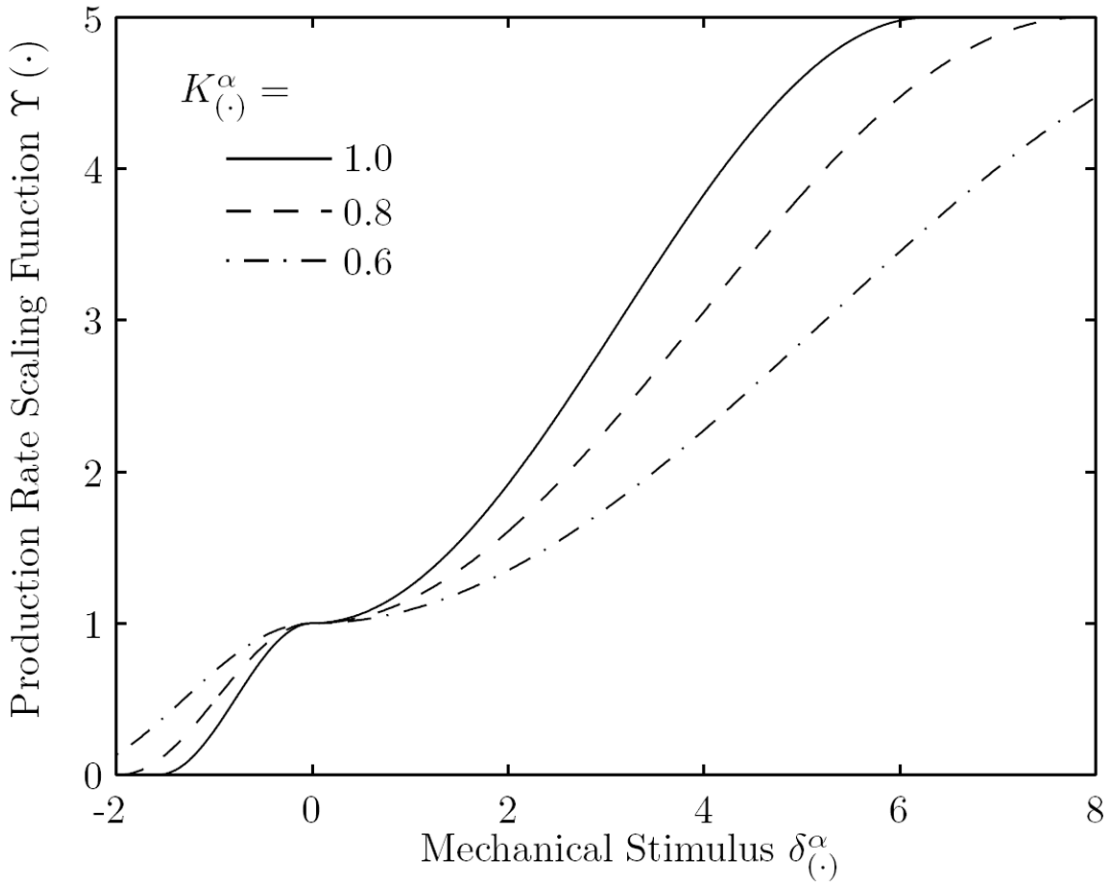


**Figure 2.**

Relationship between the mass production rate scaling function ϒ (·), described in equation (50), and normalized changes in mechanical stimuli $\delta^{\alpha}_{(\cdot)}$, for indicated values of $K^{\alpha}_{(\cdot)}$. This function recovers nearly constant, basal mass density production rates for small changes in mechanical stimuli and saturating behavior for larger changes. $K^{\alpha}_{(\cdot)}$ is the corresponding curve's maximal slope. This functional form is motivated, in part, by the growth law first put forward by Fung (1990, pg. 530).

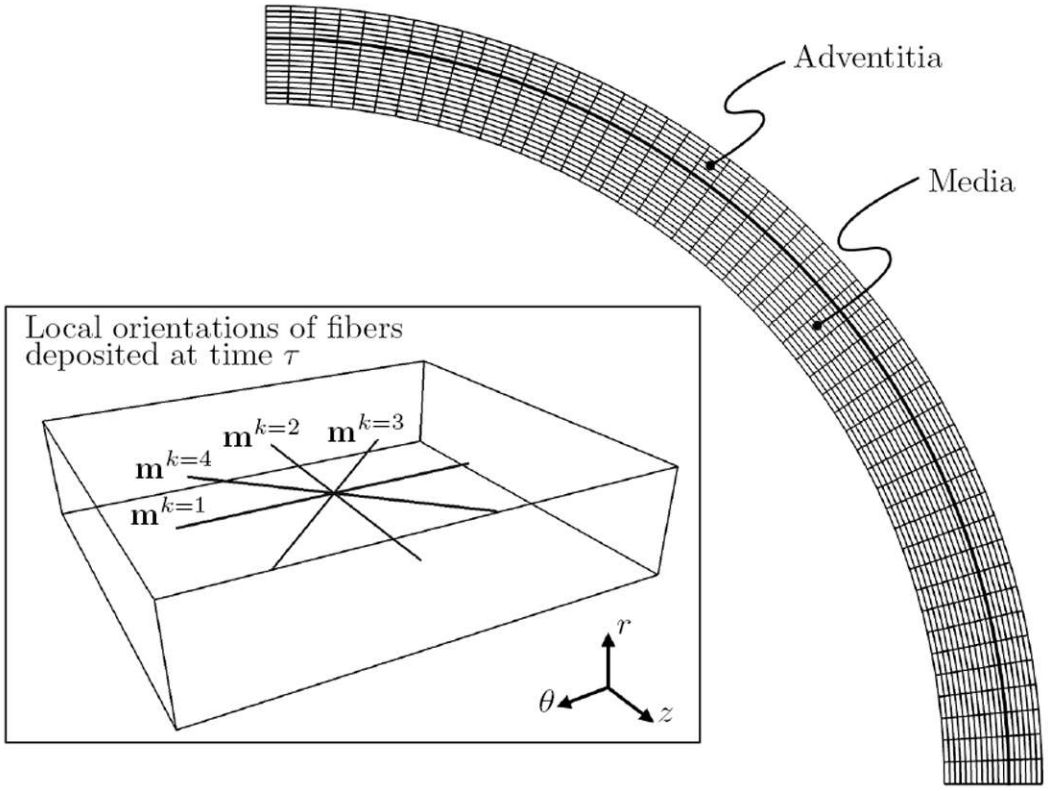


**Figure 3.**

Rendering of the quarter-symmetric finite element mesh. The inner sector represents the media and the outer sector the adventitia. The inset shows a detailed perspective view of fiber orientations within a representative element. All fibers are deposited within planes defined by the first two principal directions $\hat{\mathbf{n}}_1(\tau)$ and $\hat{\mathbf{n}}_2(\tau)$ of the deviatoric stress tensor $\boldsymbol{\sigma}_{\text{dev}}(\tau)$, which in the case of our simulated healthy artery correspond to circumferential and axial directions, respectively. Helical fibers directions $\mathbf{m}^{k=3,4}(\tau)$ are shown symmetrically oriented between circumferentially- ($\mathbf{m}^{k=1}(\tau)$) and axially- ($\mathbf{m}^{k=2}(\tau)$) aligned fibers, as described by the systems of equations (54) and (55).

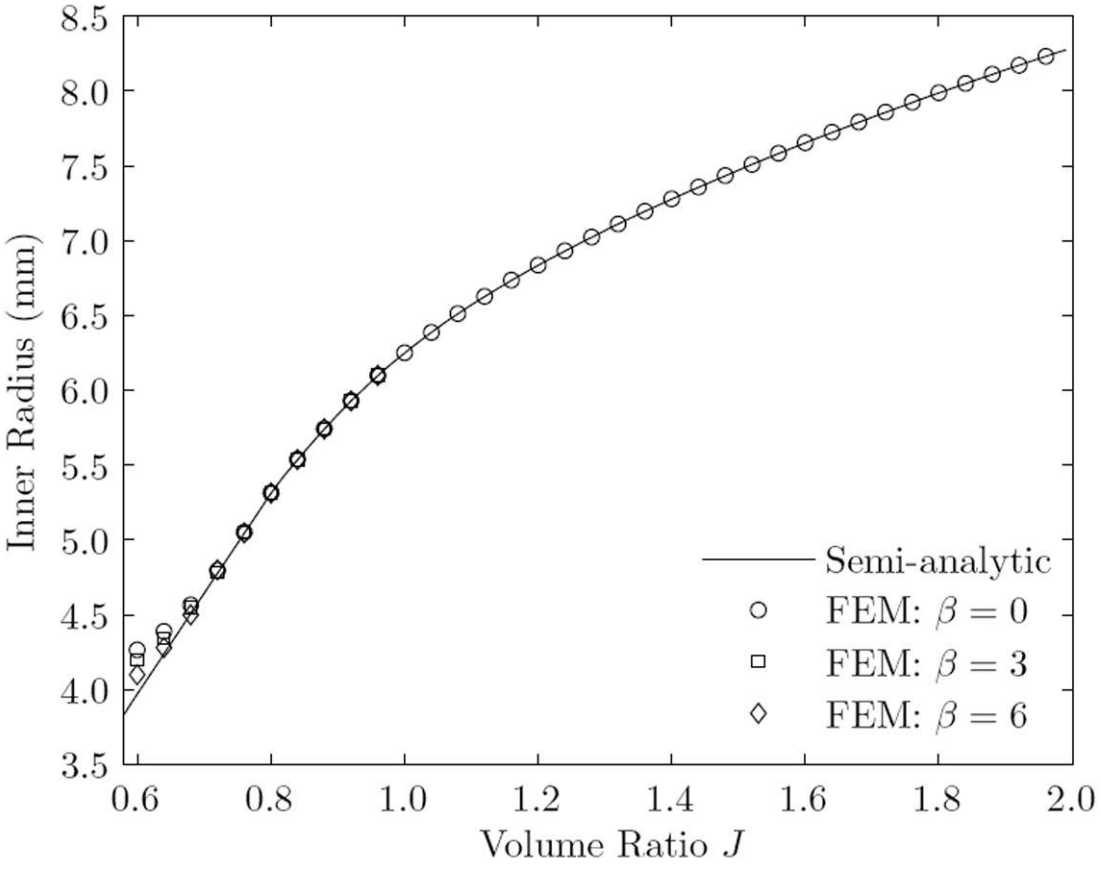


**Figure 4.**
Evolution of inner radius for the case of uniformly changing mass, and thus volume ratio $J$. Finite element results are shown by symbols for the indicated values of parameter $\beta$ (see equation (20) and figure 1), whereas results from a semi-analytic approach are shown by the solid curve. Note that for $J < 0.8$, the finite element solution improves with greater values of $\beta$.

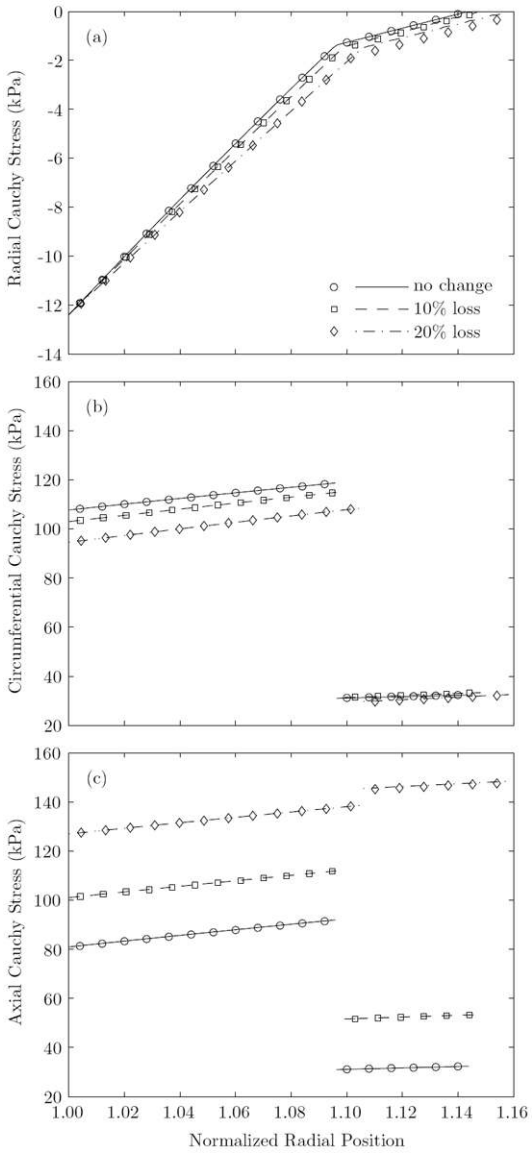


**Figure 5.**

Transmural distributions of radial (panel a), circumferential (panel b), and axial components (panel c) of Cauchy stress for the indicated degree of uniform mass loss. Radial position is normalized by the current *in vivo* inner radius. Symbols show finite element results and curves show corresponding semi-analytic results. The radial stress satisfies traction boundary conditions at the lumen (compressive luminal pressure) and outer surface (traction-free), as desired. The abrupt change in slope marks the interface between the media and adventitia as a result of their differing compositions (see table 1). Note the nearly unchanging circumferential stresses in the adventitia.

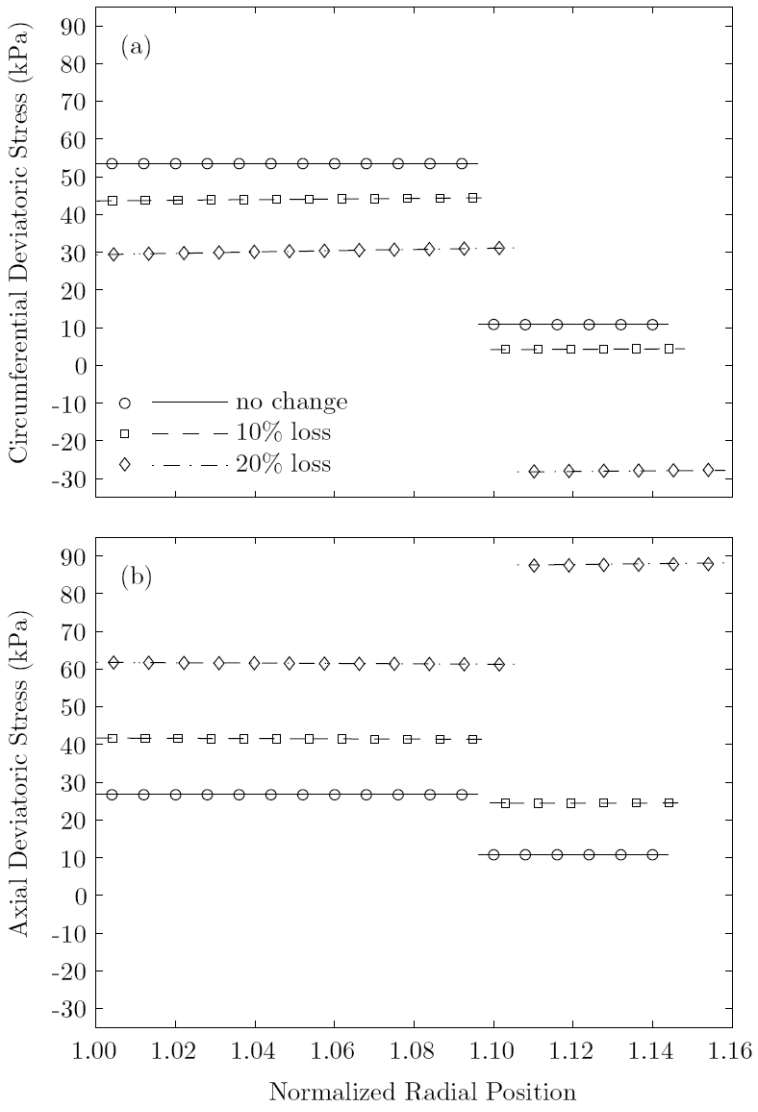


**Figure 6.**

Circumferential (panel a) and axial (panel b) deviatoric stress distributions for the indicated degree of uniform mass loss. Radial position is normalized by the current *in vivo* inner radius. Symbols show finite element results and curves show corresponding semi-analytic results. The discontinuity marks the interface between the media and adventitia. Although values vary considerably with changing mass – particularly in the adventitia – the distributions remain nearly uniform within each layer.

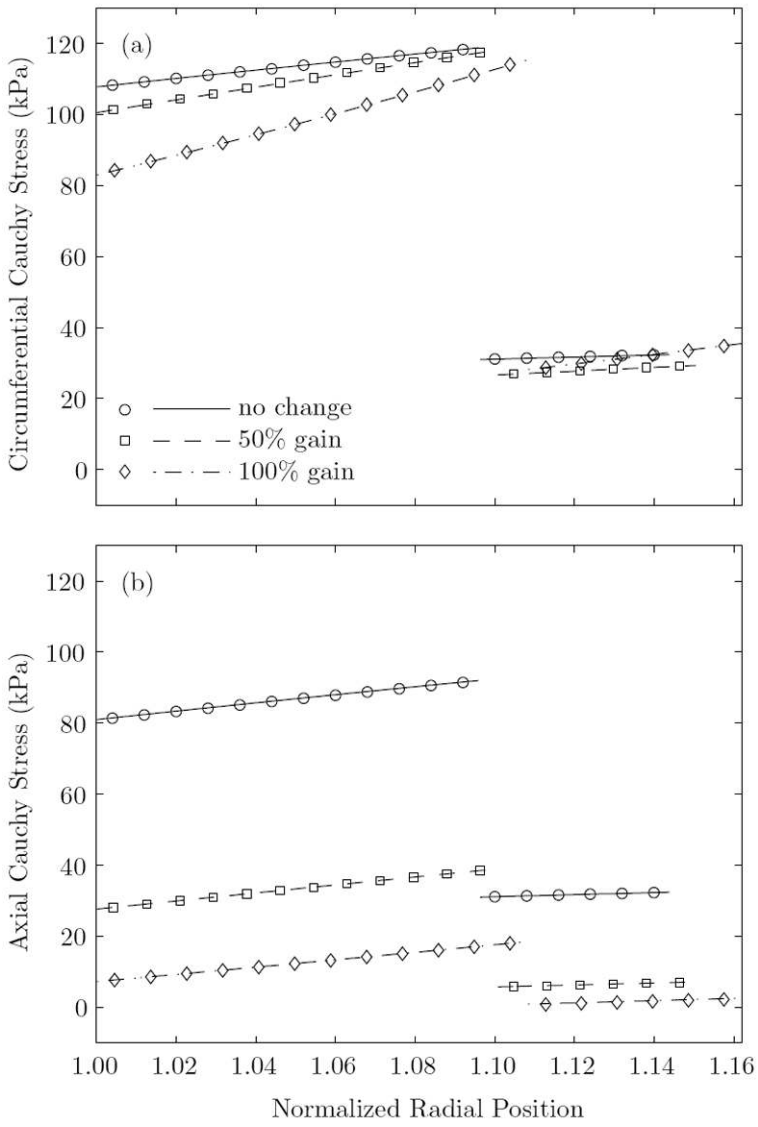


**Figure 7.**

Circumferential (panel a) and axial (panel b) Cauchy stress distributions for the indicated degree of uniform mass gained. Radial position is normalized by the current *in vivo* inner radius. Symbols show finite element results and curves show corresponding semi-analytic results. Note the nearly unchanging circumferential Cauchy stresses in the adventitia as opposed to the decreasing axial stresses.

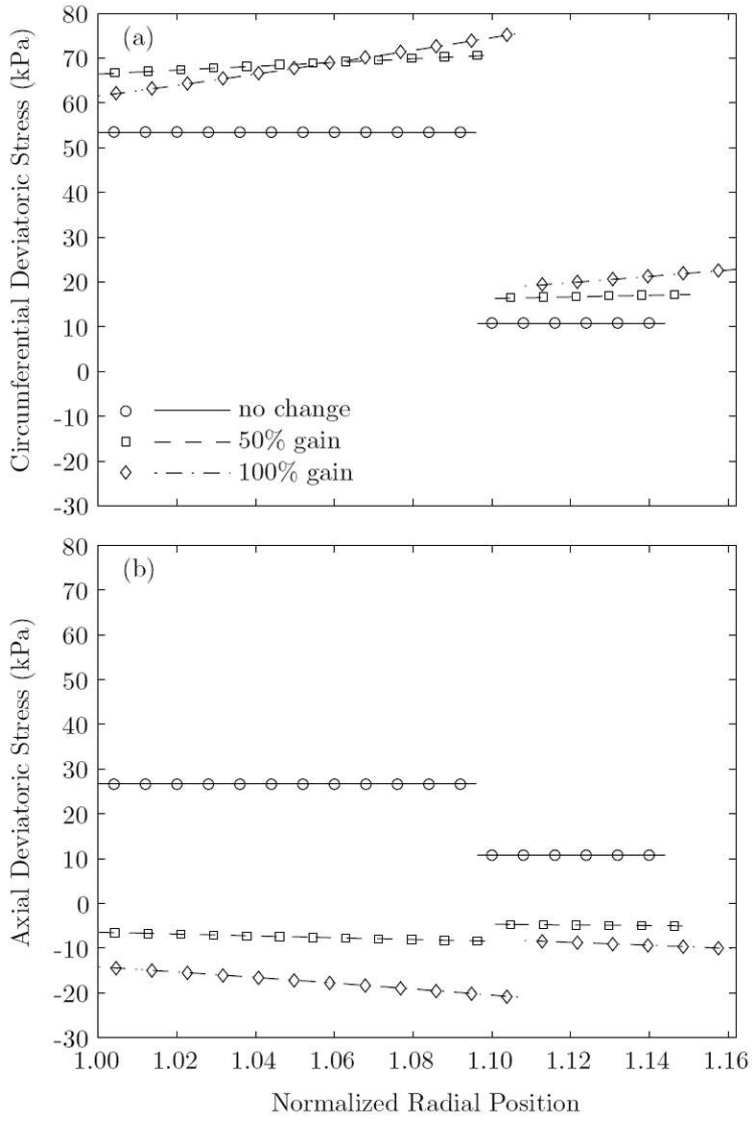


**Figure 8.**

Circumferential (panel a) and axial (panel b) deviatoric stress distributions for the indicated degree of uniform mass gained. Radial position is normalized by the current *in vivo* inner radius. Symbols show finite element results and curves show corresponding semi-analytic results. As in the case of uniform mass loss, the deviatoric stress distributions remain nearly constant within each layer, even for very large uniform increases in mass.

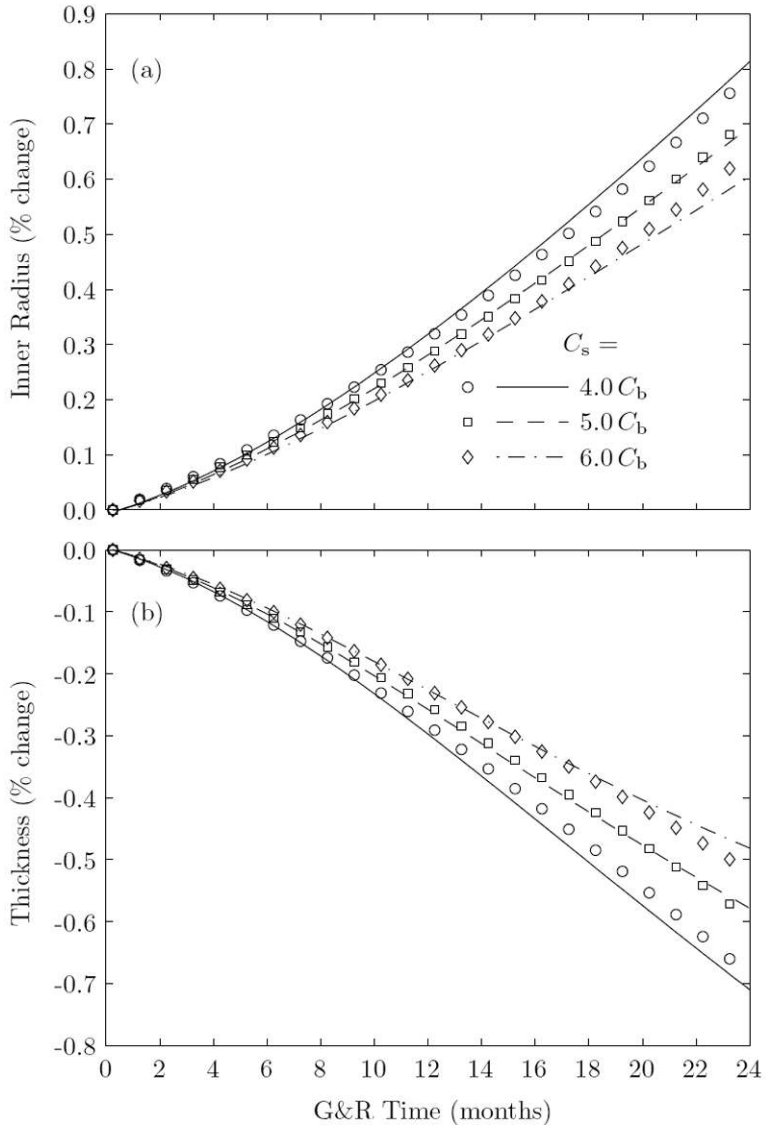


**Figure 9.**

Evolving normalized inner radius (panel a) and total wall thickness (panel b) over time for the indicated values of vaso-sensitive parameter $C_s$ (see equation (44)). Symbols show finite element results, and curves show corresponding semi-analytic results.

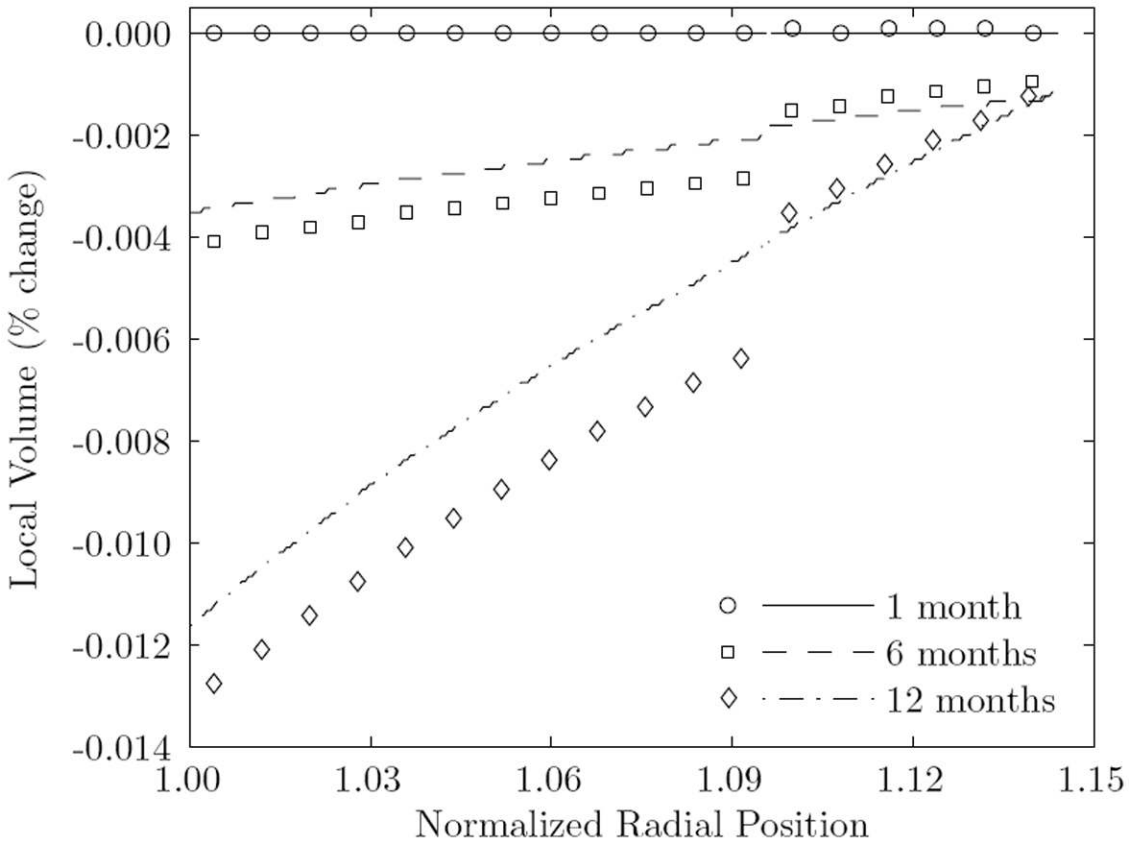


**Figure 10.**

Evolving volumes, shown over the wall thickness at the indicated G&R times, where $C_s$ = 5.0 $C_b$. Radial position is normalized by the current *in vivo* inner radius. Symbols show finite element results, and curves show corresponding semi-analytic results. The discontinuity marks the interface between the media and adventitia. Note the gradients that develop as a result of local stress-driven G&R.

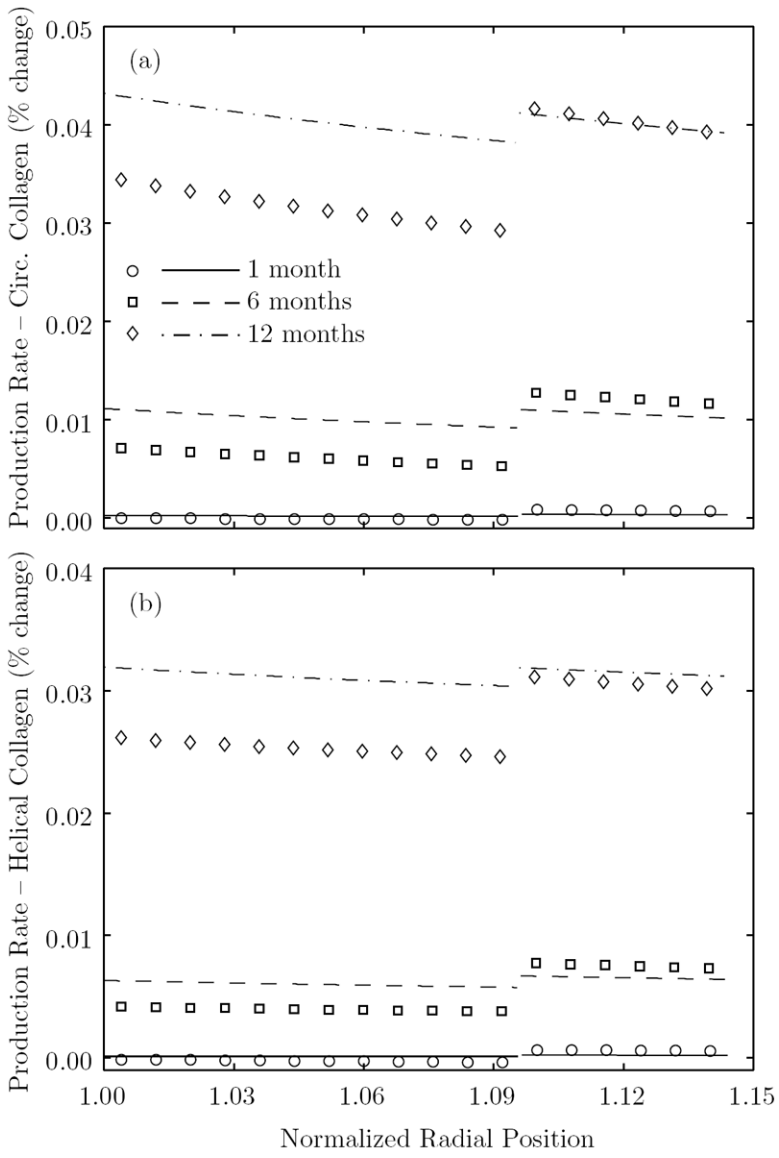


**Figure 11.**

Evolving mass density production rates for circumferentially-aligned (panel a) and helically-aligned (panel b) collagen, shown over the wall thickness at the indicated G&R times, where $C_s = 5.0\ C_b$. Radial position is normalized by the current *in vivo* inner radius. Symbols show finite element results, and curves show corresponding semi-analytic results. The discontinuity marks the interface between the media and adventitia. Differences between finite element and semi-analytic models increased with increased G&R time. Nevertheless, note that strong gradients develop as a result of local stress-driven G&R.

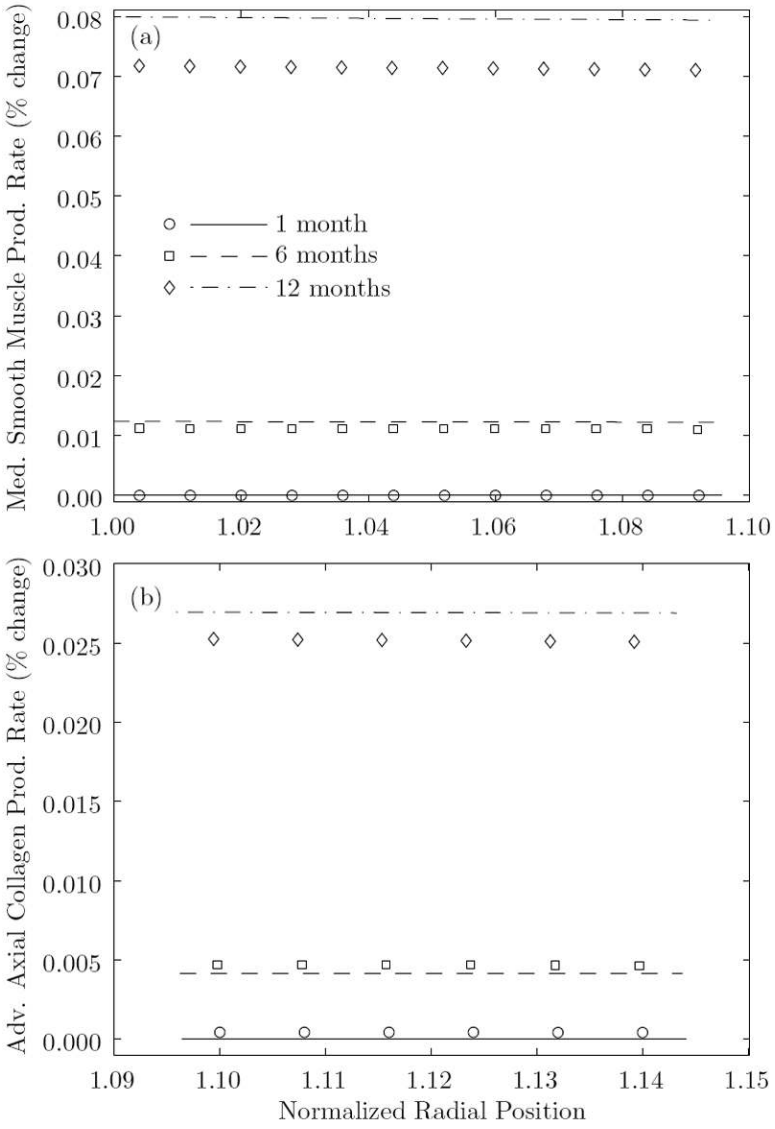


**Figure 12.**

Evolving mass density production rates for circumferentially-aligned medial smooth muscle (panel a) and axially-aligned adventitial collagen (panel b) at the indicated G&R times, where $C_s = 5.0\ C_b$. Radial position is normalized by the current *in vivo* inner radius. Symbols show finite element results, and curves show corresponding semi-analytic results. As opposed to the results shown in figure 11, the production rates for medial smooth muscle are nearly uniform at all G&R times. The driving mechanical stimulus for smooth muscle production is the deviatoric stress for muscle, which includes the active contribution. Because the active contribution does not depend on local distortions (it only depends on $C(s)$, which is a function of the wall shear stress), there is not a strong gradient in stimulus for smooth muscle production. Similarly, the production rates for axial collagen are nearly uniform at all G&R times. The driving mechanical stimulus for axially-aligned collagen is the distortional component of stress in the axial direction. Because the artery's axial length is fixed, there is not a strong gradient in stimulus for the production of axially-aligned constituents.

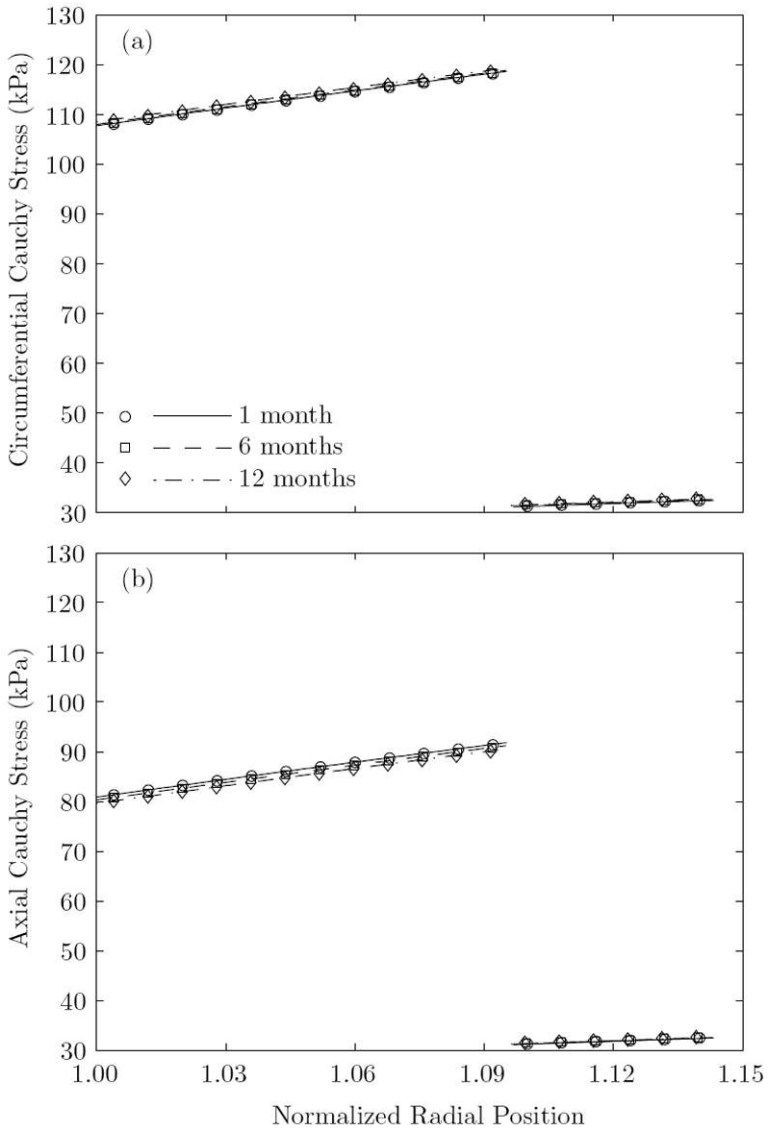


**Figure 13.**

Evolving circumferential (panel a) and axial (panel b) Cauchy stress distributions at the indicated G&R times, where $C_s = 5.0\ C_b$. Radial position is normalized by the current *in vivo* inner radius. Symbols show finite element results, and curves show corresponding semi-analytic results. The discontinuity marks the interface between the media and adventitia. The equibiaxial Cauchy stresses in the adventitia remain essentially unchanged.

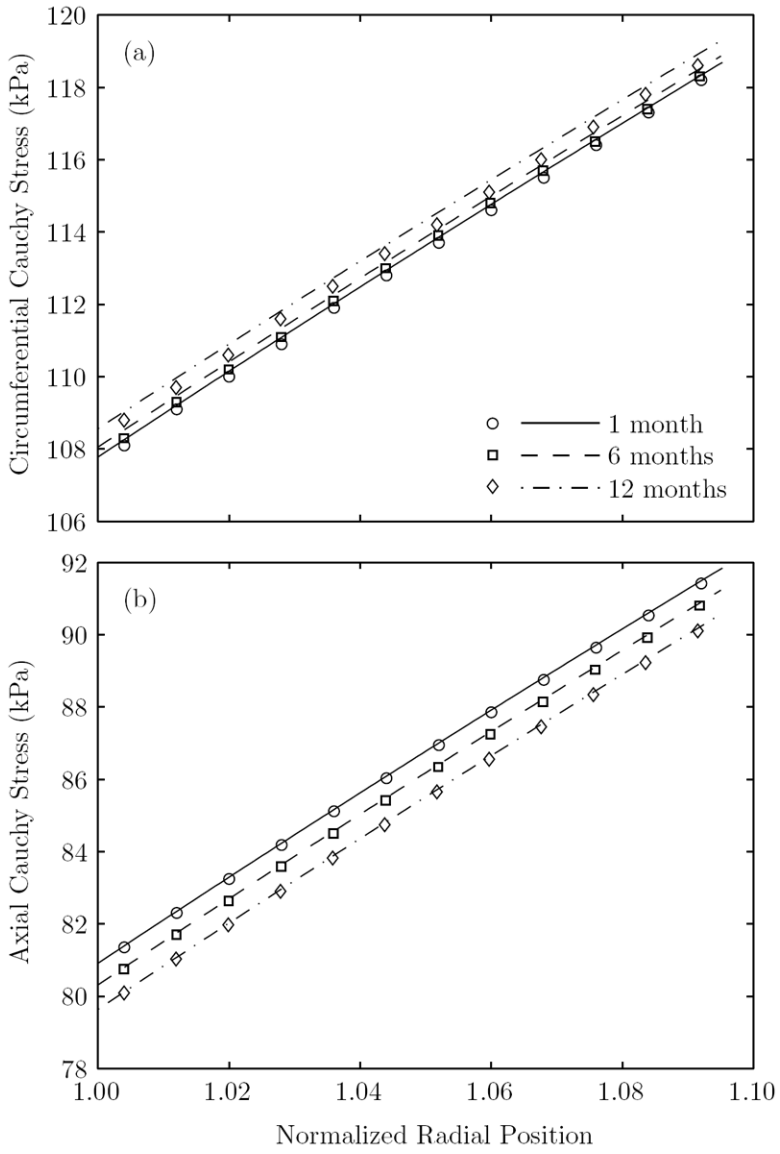


**Figure 14.**

Evolving circumferential (panel a) and axial (panel b) Cauchy stress distributions within the media at the indicated G&R times, where $C_s = 5.0\ C_b$. Radial position is normalized by the current *in vivo* inner radius. Symbols show finite element results, and curves show corresponding semi-analytic results. The ordinate axes are adjusted to exaggerate important trends obscured in figure 13. Circumferential Cauchy stresses are predicted to increase modestly as the artery distends, while the axial stresses are predicted to follow the opposite trend.

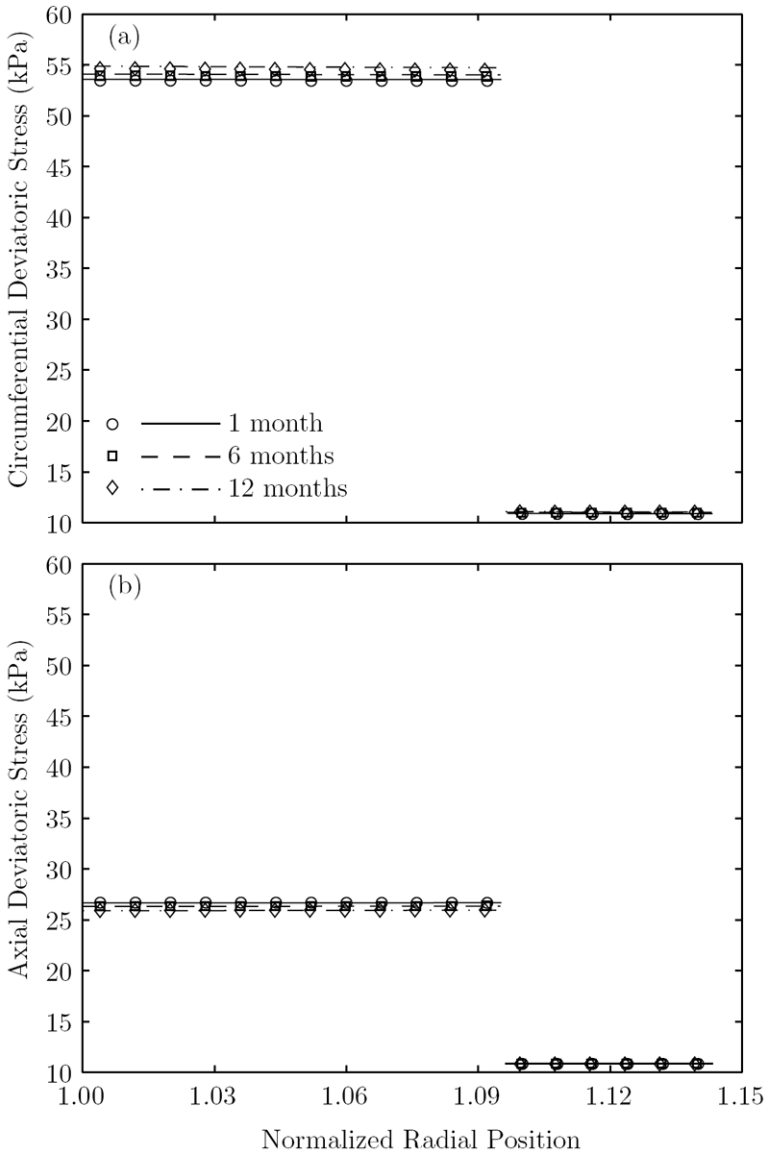


**Figure 15.**

Evolving circumferential (panel a) and axial (panel b) deviatoric stress distributions at the indicated G&R times, where $C_s = 5.0\ C_b$. Radial position is normalized by the current *in vivo* inner radius. Symbols show finite element results, and curves show corresponding semi-analytic results. The discontinuity marks the interface between the media and adventitia. The uniform equibiaxial deviatoric stresses in the adventitia remain essentially unchanged.

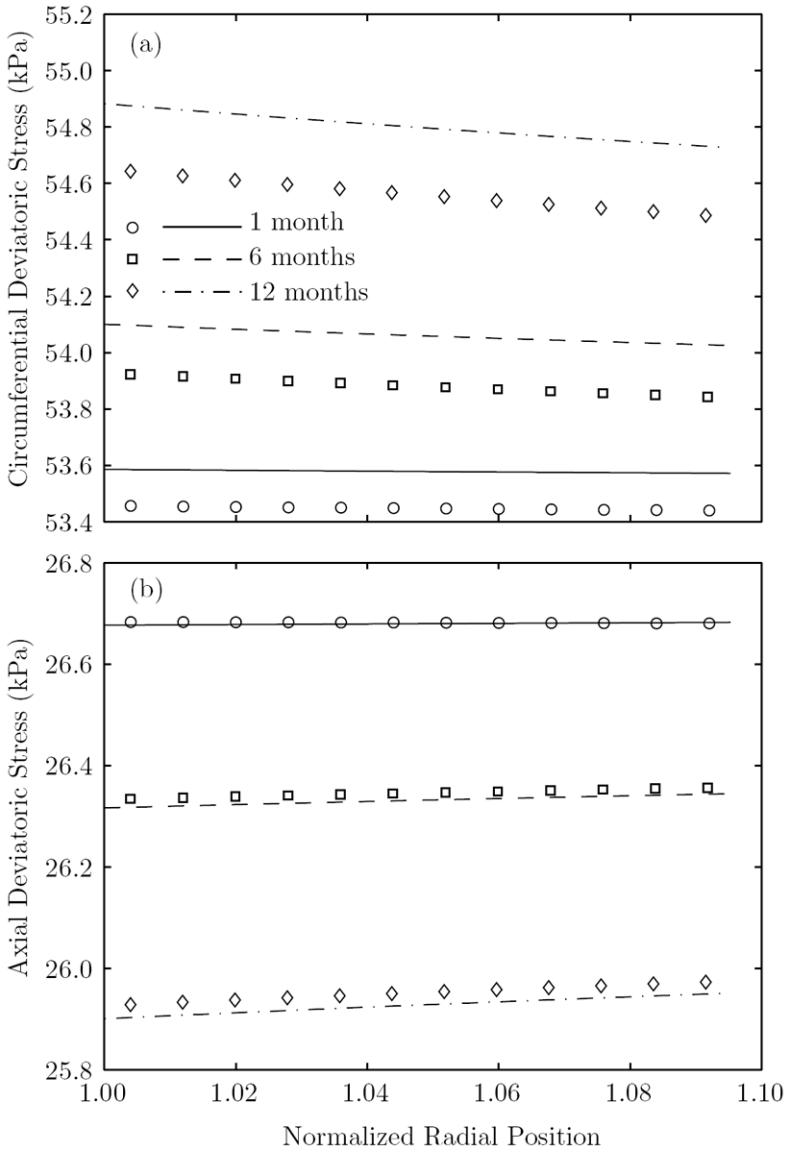


**Figure 16.**

Evolving circumferential (panel a) and axial (panel b) deviatoric stress distributions within the media at the indicated G&R times, where $C_s = 5.0\ C_b$. Radial position is normalized by the current *in vivo* inner radius. Symbols show finite element results, and curves show corresponding semi-analytic results. The ordinate axes are adjusted to exaggerate important trends which are obscured in figure 15. Note the nearly uniform deviatoric stress distributions, as compared to the strong gradients for Cauchy stress as shown in figure 14.

**Table 1**

Important parameters and their values for a representative healthy abdominal aorta. See Valentín and Humphrey (2009b) and Valentín *et al.* (2011) for detailed information regarding the motivations, roles, and bounds for such parameters.

| Class | Role | Value(s) |
|---|---|---|
| Loads/Geometries | physical constants/loads | $\rho(0) = \rho_0 = 1050 \text{kg} \cdot \text{m}^{-3}$, $\mu = 0.037 \text{ g} \cdot (\text{cm} \cdot \text{s})^{-1}$<br>$P = 93$ mmHg, $\tau_w^h = 0.5$ Pa |
| | initial loaded arterial geometry | inner radius = 6.25 mm<br>total thickness = 0.9 mm<br>medial thickness = 0.6 mm<br>adventitial thickness = 0.3 mm |
| Mechanical Parameters | passive elasticity | $c^e(0) = 125$ kPa<br>$c_2^m = 20$ kPa, $c_3^m = 1$<br>$c_2^k = 149.8$ kPa, $c_3^k = 20 \forall \overline{I_{4_{n(\tau)}}^k}(s) \in [1, \infty)$<br>$c_2^k = 0 \; \forall \overline{I_{4_{n(\tau)}}^k}(s) \in (0, 1)$ |
| | vasoactivity | $T_{max} = 300$ kPa<br>$C_b = 0.68$, $C_s \in [4, 6]\, C_b$ |
| Composition/Kinetics | deposition stretches | $\tilde{G}_{\theta\theta}^e(r), \tilde{G}_{zz}^e(r) = 1.3, G_h^k = 1.08, G_h^m = 1.2$ |
| | medial constituent fractions<br>adventitial constituent fractions | $\phi_{med}^k = 0.25, \phi_{med}^e = 0.55, \phi_{med}^m = 0.2$<br>$\phi_{adv}^k = 0.95, \phi_{adv}^e = 0.05, \phi_{adv}^m = 0.0$ |
| | medial collagen fractions | $\phi_0^k = 0.8\, \phi_{med}^k, \phi_{helical}^k = 0.2\, \phi_{med}^k, \phi_z^k = 0$ |

| Class | Role | Value(s) |
|---|---|---|
| | adventitial collagen fractions | $\phi^k_\theta=0.1\ \phi^k_{\text{adv}}, \phi^k_{\text{helical}}=0.8\ \phi^k_{\text{adv}}, \phi^k_z=0.1\ \phi^k_{\text{adv}}$ |
| | homeostatic kinetics | $K^{\text{m}}_{q_{\text{h}}}, K^m_{q_{\text{h}}}=\ln(2)/70\ \text{days}^{-1}$<br>$K^{\text{e}} = \ln(2)/14600\ \text{days}^{-1}$ |
| | production kinetics | $m^\alpha_{\max}=5$<br>$K^\alpha_\sigma=1.0, K^\alpha_{\tau_{\text{w}}}=1.0$ |



*Int j numer method biomed eng*. Author manuscript; available in PMC 2014 August 01.